

IMPROVEMENTS TO THE ELECTROHYDRODYNAMIC JET PRINTING PROCESS

BY

SARAH MANNEN

THESIS

Submitted in partial fulfillment of the requirements
for the degree of Master of Science in Mechanical Engineering
in the Graduate College of the
University of Illinois at Urbana-Champaign, 2013

Urbana, Illinois

Adviser:

Professor Andrew Alleyne

Abstract

Significant interest has been developed in micro- and nano-scale manufacturing in recent years, and Electrohydrodynamic Jet (E-Jet) printing offers unique advantages over other technologies in this field. In this thesis, we describe two individual improvements to E-jet printing which will increase its capabilities for micro- and nano-scale manufacturing. First, an investigation into new silver nanoparticle inks for use in electronics printing yielded 4-20 μm lines with resistivities around ten times that of bulk silver. The printed performance is demonstrated to be promising for microscale additive manufacturing. Specific obstacles and solutions unique to E-jet printing of conductive inks which are presented here so as to be useful in ink selection and tuning. Secondly, we also present a gray-box switched-system model for the trajectory of a jet during the printing process which accurately captures features observed through high-speed imaging. This model is simple and flexible enough to be useful for variety of applications. The contributions presented in this thesis are intended to advance E-jet technology for both academic and commercial use.

To my family.

Acknowledgements

This work would not have been possible without the support of many individuals along the way. First, I would like to thank my research advisor, Dr. Andrew Alleyne, for his guidance in both technical areas and personal development. He has encouraged me to think critically and continually expand my knowledge into new fields. I also greatly appreciate the members of the Alleyne Research Group for their assistance and camaraderie, and would particularly like to thank Erick Sutanto for giving me an introduction to E-jet printing.

To the members of the NanoCEMMS E-jet group: your advice and criticism helped me to clarify the goals of my research and overcome many challenges. In particular, I would like to thank Dr. Ferreira, Dr. Rogers, and Dr. Wagoner Johnson.

The silver printing work presented in this thesis would not have been possible without the support of Dr. Yuri Didenko and the UT Dots company. Thank you for providing your ink and your invaluable expertise in materials. I have learned a great deal from our collaboration.

Many other individuals at the University of Illinois have provided me with assistance and answered my questions during the past two years. Although it is not possible to address each one, I would like to acknowledge the help I received from Dan Block, Leilei Yin, Dr. Randy Ewoldt, and SukWon Hwang.

I would like to thank my parents, Dean and Johna Mannen, for teaching me the value of education and intellectual curiosity and giving me tremendous love and support over the years. I feel very lucky to have you both. Thanks to all of my family and friends, and especially to Joey Fasl, who has been so understanding and encouraging over the past two years.

Table of Contents

CHAPTER	Page
LIST OF TABLES	vii
LIST OF FIGURES	viii
LIST OF SYMBOLS	xii
CHAPTER 1 INTRODUCTION	1
1.1 Micro- and Nano-Manufacturing	1
1.2 Electrohydrodynamic Jet Printing	1
1.3 Thesis Organization.....	3
CHAPTER 2 SILVER INK PRINTING.....	5
2.1 Conductive Ink Printing	5
2.2 Ink Description	8
2.3 Printing and Annealing Methodology	9
2.4 Challenges	10
2.5 Results	18
2.6 Conclusions and Future Work	28
CHAPTER 3 SINGLE DROP MODELING AND VALIDATION.....	31
3.1 E-Jet Modeling Background.....	31
3.2 Development of Jetting Model Structure	32
3.3 Imaging with High-Speed Camera	37
3.4 Model Parameter Determination	47

3.5 Summary	58
CHAPTER 4 JET CYCLE MODELING AND VALIDATION	59
4.1 Introduction	59
4.2 Three-Mode Switched-System Model.....	60
4.3 Single-Mode Switched-System Model.....	70
4.4 Summary and Future Work	77
CHAPTER 5 CONCLUSIONS	79
5.1 Summary	79
5.2 Conclusions	80
5.3 Future Work	81
LIST OF REFERENCES	83

List of Tables

Table 2.1 Summary of resistance, geometry, and resistivity of silver lines printed with E-jet.	27
Table 3.1 Coefficients for discrete model determined using batch least squares method.	50
Table 3.2 Parameter ratios for mass-spring-damper model calculated from discrete coefficients.	51
Table 3.3 Tuned parameter ratios for mass-spring-damper model.	53
Table 4.1 Parameter ratios during retraction mode for all drops in jetting cycle.	61
Table 4.2 Rates of change of parameter ratios during first and second build modes.	64
Table 4.3 Parameter ratio values during first, second, and third drop modes of a jetting cycle.	66
Table 4.4 Derivatives of parameter ratios during first, second, and third drop modes of a jetting cycle.	71
Table 4.5 Initial conditions for parameter ratios in first, second, and third drop modes of a jetting cycle.	72

List of Figures

Figure 1.1 Schematic of E-jet printer [13].	3
Figure 2.1 Summary of resistivity and width of printed conductive lines reported in the literature.	8
Figure 2.2 Diagram of printing pattern for line with pads.	9
Figure 2.3 Breaks between lines and pads of AgDDB due to reflow of ink during annealing.	12
Figure 2.4 AgHB on Teflon showing line breaks due to poor wettability of substrate.	14
Figure 2.5 AgHB line exhibiting coffee ring effect in (a) optical microscope image and (b) AFM height measurement plot.	15
Figure 2.6 Illustration of the coffee ring effect: (a) solvent evaporation, (b) ink flow to replace lost solvent at edges, (c) buildup of solute at edges as solvent evaporates.	16
Figure 2.7 Optical microscope image of 20-pass AgHB line (10% w/v Ag) printed with 5 μm nozzle after annealing.	19
Figure 2.8 Optical microscope image of 10-pass AgDDB line (25% w/v Ag) printed with 5 μm nozzle after annealing.	19
Figure 2.9 Optical microscope image of 20-pass AgDDB line (25% w/v Ag) printed with 5 μm nozzle after annealing.	20
Figure 2.10 Optical microscope image of 20-pass AgDDB line (50% w/v Ag) printed with 5 μm nozzle after annealing.	20
Figure 2.11 Optical microscope image of 25-pass AgDDB line (50% w/v Ag) printed with 2 μm nozzle after annealing.	21
Figure 2.12 Current measurements during voltage sweep for 20- and 30-pass AgHB (10% w/v Ag) lines printed with 5 μm nozzle used to calculate resistance.	21
Figure 2.13 Current measurements during voltage sweep for 10- and 20-pass AgDDB (25% w/v Ag) lines printed with 5 μm nozzle used to calculate resistance.	22
Figure 2.14 Current measurements during voltage sweep for 20-pass AgDDB (50% w/v Ag) lines printed with 5 μm nozzle used to calculate resistance.	22

Figure 2.15 Current measurements during voltage sweep for 25-pass AgDDB (50% w/v Ag) lines printed with 2 μm nozzle used to calculate resistance.	23
Figure 2.16 Adjusted height measurements for a single line scan of 30-pass AgHB.....	24
Figure 2.17 AFM height measurements for 20-pass AgHB (10% w/v Ag) printed with 5 micron nozzle.	25
Figure 2.18 AFM height measurements for 20-pass AgHB (10% w/v Ag) printed with 5 micron nozzle.	25
Figure 2.19 AFM height measurements for 25-pass AgDDB (50% w/v Ag) printed with 2 micron nozzle.	26
Figure 2.20 Comparison of resistivity and width of printed conductive lines reported in the literature to lines printed in the current work.	29
Figure 2.21 Comparison of resistivity and width of printed conductive lines reported in the literature to lines printed in the current work (detail view).	29
Figure 3.1 Diagram of jet modeled as a mass connected to the nozzle by a spring and damper.....	34
Figure 3.2 Free-body diagram of the forces acting on the jet tip.	34
Figure 3.3 Method of image charges used to describe the electrical field due to a jet produced by a single nozzle above a grounded substrate.	36
Figure 3.4 Method of image charges used to describe the electrical field due to jets produced by multiple nozzles above a grounded substrate.....	36
Figure 3.5 Image captured using a standard CCD camera with a rolling shutter and a strobe light. ...	39
Figure 3.6 Schematic of signal generation for strobe imaging.	40
Figure 3.7 Frames from high-speed video of one jetting cycle of a 50% water/50% glycerol solution from a 10 μm nozzle.	41
Figure 3.8 Frames from high-speed video of one jetting cycle of a 75% water/25% glycerol solution from a 10 μm nozzle.	41
Figure 3.9 Frames from high-speed video of one jetting cycle of NOA74 from a 5 μm nozzle.....	42
Figure 3.10 Frame from high-speed video before and after cropping to desired region.	43
Figure 3.11 Conversion of grayscale image to binary image.	44
Figure 3.12 Distance/pixel scale factor determination.	44
Figure 3.13 Definition of z_0 , z_s , and $+z$ direction.	45
Figure 3.14 Height z of jet tip during one full jetting cycle of NOA 74 with a 5 micron nozzle.....	46
Figure 3.15 Average height z of jet tip at each sample time for all test samples of NOA 74 with a 5 micron nozzle. Error bars represent one standard deviation above and below the mean.	47

Figure 3.16 Height z of jet tip during a single drop simulation using average calculated parameter ratios.	52
Figure 3.17 Height z of jet tip during a single drop from data and simulations using calculated or tuned parameters.	54
Figure 3.18 Height z of jet tip during a single drop from data and simulation using physical property-based modeling.	57
Figure 4.1 Diagram of three-mode jet cycle.....	60
Figure 4.2 Illustration of drop, retraction, and build modes with height data from Test 5.....	60
Figure 4.3 Height z of jet tip during a full jetting cycle from data and simulation using three-mode parameter model with build rates chosen to keep parameter ratios continuous across modes. ...	63
Figure 4.4 Parameter ratios during full jetting cycle simulation using drop, retraction, and build modes. Parameter ratios are continuous from retraction to build mode and from build mode to drop mode.	64
Figure 4.5 Parameter ratios during full jetting cycle simulation using drop, retraction, and build modes. Parameter ratios have discontinuities between modes.	65
Figure 4.6 Stateflow diagram for determination of parameter ratio values during full jetting cycle with multiple drop, retraction, and build modes.	67
Figure 4.7 Height z of jet tip during a full jetting cycle from data and simulation using three-mode parameter model.	68
Figure 4.8 Comparison of height of jet tip during a full jetting cycle from simulation using three-mode parameter model and mean height during all data sets with error bars representing one standard deviation above and below the mean.	69
Figure 4.9 Illustration of single (drop) mode occurring multiple times during a jetting cycle.	70
Figure 4.10 Stateflow diagram for determination of parameter ratio values during full jetting cycle with continuously changing parameter ratios.	73
Figure 4.11 Parameter ratios during full jetting cycle simulation with three drop modes.	73
Figure 4.12 Height z of jet tip during a full jetting cycle from data and simulation using single-mode parameter model.	74
Figure 4.13 Comparison of height of jet tip during a full jetting cycle from simulation using single-mode parameter model and mean height during all data sets with error bars representing one standard deviation above and below the mean.	75
Figure 4.14 Height of jet tip during all seventeen jetting cycle tests with upper and lower bounds of data indicated by dashed line.	76

Figure 4.15 Comparison of height of jet tip during a full jetting cycle from simulation using single-mode parameter model and upper and lower bounds for envelope of data from all test runs.	77
Figure 5.1 Demonstration of silver interconnects printed with E-jet, (a) showing magnified LED and interconnects and (b) showing LED response to voltage difference applied across printed pads.	81

List of Symbols

A	Cross-Sectional Area	m^2
b	Damping Coefficient	$\text{N} \cdot \text{s} \cdot \text{m}^{-1}$
c	Coulomb's Constant	$\text{N} \cdot \text{m}^2 \cdot \text{C}^{-2}$
F_b	Damping Force	N
F_d	Drag Force	N
F_e	Electrical Force	N
F_g	Gravitational Force	N
F_k	Spring Force	N
F_γ	Surface Tension Force	N
$F_{\eta e}$	Extensional Viscosity Force	N
g	Gravitational Acceleration	$\text{m} \cdot \text{s}^{-2}$
k	Spring Constant	$\text{N} \cdot \text{m}^{-1}$
L	Characteristic Length	m
l	length	m
m	Mass	kg
q	Charge	C
R	Resistance	Ω
r	Radius	m
Re	Reynolds Number	--
T	Sampling Period	s
U	Artificial Input	m^{-2}
U^*	Modified Artificial Input	m^{-2}

v	velocity	$\text{m} \cdot \text{s}^{-1}$
z	Distance from Nozzle to Jet Tip	μm
z_0	Initial Position of Jet Tip	μm
z_s	Position of Substrate Relative to Nozzle	μm
γ	Surface Tension	$\text{N} \cdot \text{m}^{-1}$
$\dot{\epsilon}$	Strain Rate	s^{-1}
η_e	Extensional Viscosity	$\text{Pa} \cdot \text{s}$
θ	Vector of Coefficients	--
ρ	Resistivity	$\Omega \cdot \text{m}$
ρ_d	Density	$\text{kg} \cdot \text{m}^{-3}$
σ_n	Normal Stress	Pa
τ	Time Constant	s
Φ	Regression Vector	--

Chapter 1

Introduction

1.1 Micro- and Nano-Manufacturing

Manufacturing has traditionally made up a large portion of the U.S. economy [1]. Due to increased competition in the manufacturing sphere over the last several years, more traditional forms of manufacturing have often been outsourced to other countries. The U.S. has, however, continued to excel in more high-tech, specialized areas [2]. One area in particular which has been gaining importance in recent years is micro- and nano-manufacturing.

Micro- and nano-manufacturing refers to the process of creating devices or products on the scale of 10^{-6} to 10^{-9} meters. Some examples of current micro- and nano-manufacturing technologies include several types of lithography [3], transfer printing [4] and inkjet printing [5]. The interest in micro- and nano-manufacturing can be attributed to several factors, but one of the primary reasons is the reduction in size of electronic devices. The production of smaller electronic devices means that some features must be a few microns or even a few nanometers in size. Some of the applications in the field of electronics include transistors, LEDs, RFID chips, and memory devices [6]. Aside from electronics, micro- and nano-manufacturing is also important for biological applications including sensors [7].

1.2 Electrohydrodynamic Jet Printing

Electrohydrodynamic jet (E-jet) printing involves the application of a voltage difference between a nozzle containing ink and a substrate. The applied voltage creates an electric field which changes the shape of the meniscus to form a Taylor cone [8]. When the force due to the

electrical field exceeds the surface tension force holding the ink to the nozzle, a jet is produced from the tip of the cone. This jet creates deposits ink onto the substrate.

E-jet printing offers several benefits over other micro- and nano-manufacturing methods. E-jet printing is an additive manufacturing technology, meaning that material is directly added to the substrate in desired locations rather than coating the entire substrate and removing the ink from all areas except the desired locations. This is beneficial for two reasons: first, it requires less ink to create patterns, which reduces the material cost; second, because no excess ink is deposited, less waste is generated. Many inks are hazardous to the environment, so reducing the amount of waste generated also reduces the environmental impact of the manufacturing process. E-jet printing has been demonstrated on a wide variety of substrates, including flexible substrates [9]. The ability to print on flexible substrates is crucial for the development of devices such as “skin” pressure sensors [10] and flexible OLED displays [11]. The previous benefits can also be provided by inkjet printing. However, the size of inkjet-printed features is fundamentally limited by the size of the nozzles used for printing. In contrast, because the jet produced using the E-jet emanates from the tip of the Taylor cone, the jet produced may be much smaller than the nozzle used to print [12].

The experiments described in this work were conducted using the E-jet printer at the University of Illinois described in [13] and illustrated in Figure 1.1. The ink is contained in a chamber in which the pressure may be controlled. The chamber is connected to a glass nozzle with a tip which, for this study, has 2-10 μm inner diameter. The nozzle is sputter-coated with a gold-palladium alloy to make it electrically conductive. A voltage, in our case approximately 250-400 V, is applied to the nozzle to generate an electric field which produces a jet. The substrate is mounted on a five-axis, high-precision stage, and the standoff height from the nozzle to the substrate is typically 20-30 μm in this work.

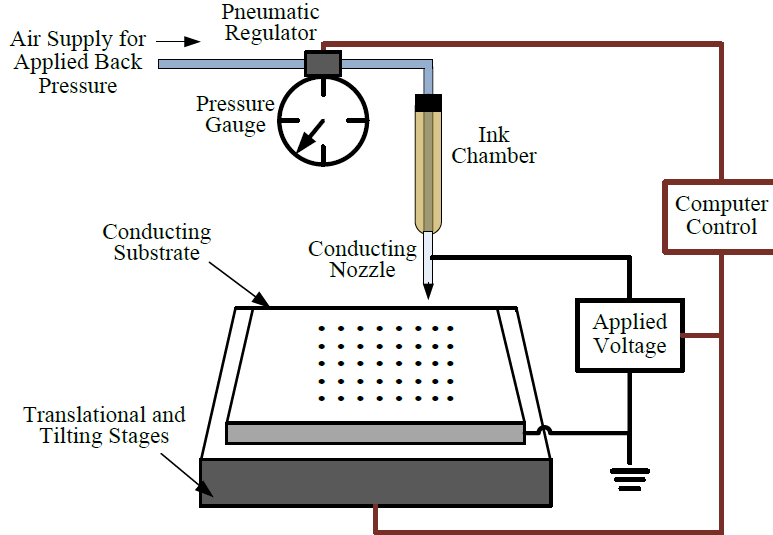


Figure 1.1 Schematic of E-jet printer [13].

Previous researchers at the University of Illinois have made advances in E-jet printing. Some of these include the development of a desktop-scale E-jet system [14] and printing with multiple nozzles and multiple materials [15]. Other research groups have demonstrated E-jet printed electronic devices and have developed models for particular aspects of E-jet printing including jetting frequency [16] and droplet size [17].

1.3 Thesis Organization

The goal of the work presented in this thesis is to provide improvements to the E-Jet printing process. These improvements are focused on two areas: conductive ink printing and modeling of the trajectory of a jet. In this introductory chapter, we have explained the need for micro- and nano-manufacturing in general. We have also presented the principles behind E-jet printing, described the benefits of E-jet as compared to other manufacturing technologies, and reported on some of the recent research in the field.

In Chapter 2, we discuss issues related to printing conductive inks for use in printed electronics. This chapter describes some of the challenges encountered while printing with silver nanoparticle inks as well as solutions or ways to avoid those problems. Images and resistivity calculations are given for two types of silver inks developed by UT Dots, Inc. The size and

resistivity of the lines developed in this work is discussed in the context of other results in the literature.

In Chapters 3 and 4, we develop a gray-box model for the multiple-drop jetting cycle based on a simplified mass-spring-damper analogy. The model determines the vertical position of the jet tip as the jet extends and retracts from the nozzle to the substrate. The third chapter focuses on a single drop, explaining the process of parameter selection based on least-squares fitting to data collected from high-speed imaging of the jetting cycle. The fourth chapter extends the model to describe the full, multiple drop jetting cycle by presenting two methods of mode switching which govern the values of the system parameters. The validity of these modeling methods are assessed by comparing the simulation results to data from seventeen separate jetting cycles.

In Chapter 5, we conclude with a summary of the contributions made in the areas of conductive ink printing and jet cycle modeling. Ideas for future work which can expand on and further improve the research presented in this thesis are also discussed.

Chapter 2

Silver Ink Printing

2.1 Conductive Ink Printing

2.1.1 Motivation

Electronics have been steadily decreasing in size for a number of years due to innovation in materials and manufacturing methods as well as circuit design. In the area of transistors on integrated circuits specifically, this phenomenon was described by Gordon Moore in his famous observation that the number of components doubles every year [18]. In order for this trend to continue, the size of both electronic devices and the conductive traces which connect them together must be reduced.

As mentioned in the introduction to this study, one of the reasons E-jet holds such great potential as a method of manufacturing is that it provides the capability to print smaller features than are possible using other methods. E-jet has been used to produce features on the order of hundreds of nanometers [9], so printing conductive traces of width 10 μm or less is a task which this method can be expected to perform well. However, the ink itself introduces other concerns, including conductive performance at a small scale and printability with small nozzles. Inks which work well at larger scales can be problematic when the feature size is reduced.

While printing of conductive inks has been demonstrated using both inkjet and E-jet, the goal of this study is to select and demonstrate printing of an ink which can be used to print narrow lines, specifically less than 10 μm in width, which exhibit low resistivity. Additionally, this work describes ink and process characteristics which lead to successful printing as well as challenges which must be overcome in order to print conductive inks using E-jet.

2.1.2 State of the Art

2.1.2.1 Inkjet Printing

Because inkjet is an older manufacturing technology than E-jet, it has been more widely used to print conductive inks. Conductive inks designed to be printed with inkjet are commercially available, and printing procedures have been tuned to create smooth lines of predictable width.

Conductive traces printed with inkjet have reached the fundamental size limitation of the technology. While this feature size is currently sufficient for most applications, it does not allow for a reduction in size of electronic circuits. H.H. Lee et. al. demonstrated lines of width 130 μm and resistivity $1.6 \times 10^{-7} \Omega\cdot\text{m}$ [19]. In 2009, D. Kim et. al. reported silver traces of width 46 μm with resistivity $2 \times 10^{-7} \Omega\cdot\text{m}$ [20]. More recently, C. Kim et. al. demonstrated lines of varying widths [21]. For the lines which were wider than 0.4 mm, the resistivity was $3.6\text{-}5.4 \times 10^{-8} \Omega\cdot\text{m}$. For lines narrower than 0.3 mm, a resistivity of $3.9\text{-}4.2 \times 10^{-8} \Omega\cdot\text{m}$ was achieved with a gradual annealing process. The resistivity reported for inkjet-printed lines is approximately 2-13 times that of bulk silver. This can be attributed to the high quality of the lines (lack of defects) and the well-developed printing and annealing procedures which lead to the removal of nearly all solvent and surfactants from the printed ink.

Conductive inks have been printed not only on rigid substrates such as silicon or glass, but also on flexible substrates [22]. The ability to print on flexible substrates is important in certain types of electronics, including some touch screens and displays [23].

Some of the applications of conductive ink printing with inkjet include transistors [24], [25], and RFID components [22].

2.1.2.2 E-jet Printing

To our knowledge, there are currently no commercial sources of conductive ink designed specifically for use with E-jet printing. Instead, some researchers have adapted inks designed for inkjet printing, while others have fabricated their own inks. These inks typically have many similarities to inkjet inks: they consist of nanoparticles in some type of solvent. The nanoparticles are surrounded by a surfactant to stabilize them in solution, i.e., prevent them from aggregating into large clumps.

Most E-jet researchers use nozzles which have tip diameters on the order of tens or even hundreds of microns in combination with nozzle-to-substrate standoff heights around 1 mm and larger voltages applied to the nozzle. The features which have been produced therefore are often comparable to inkjet-printed features in size. The resistivity achieved to date with E-jet conductive traces is also comparable to that of inkjet traces. Lee et. al. printed lines a few hundred nanometers in width with resistivity $4.8 \times 10^{-8} \Omega\cdot\text{m}$ [26]. Khan et. al. reported silver lines of width $140 \mu\text{m}$ and resistivity $5.05 \times 10^{-8} \Omega\cdot\text{m}$ [27].

There are some examples of complete devices and applications of conductive ink printing in the E-jet literature. Khan et. al. printed a thin-film transistor using E-jet with contact electrodes made with colloidal silver ink [28]. Choi et. al. demonstrated a memristive device with silver electrodes [29].

In 2008, Sekitani et. al. reported printing $2 \mu\text{m}$ -wide lines of silver ink which were used in the development of small-scale transistors [30]. To our knowledge, these are the narrowest conductive lines which have been printed. The resistivity of these lines was $2.5 \times 10^{-7} \Omega\cdot\text{m}$. In this work, we report E-jet printing of lines with slightly larger width but lower resistivity.

Figure 2.1 summarizes results from the literature regarding width and resistivity of conductive lines printed with inkjet and E-jet. The values reported above along with other results from [31], [32], [33], [34], and [35] are included in the plot.

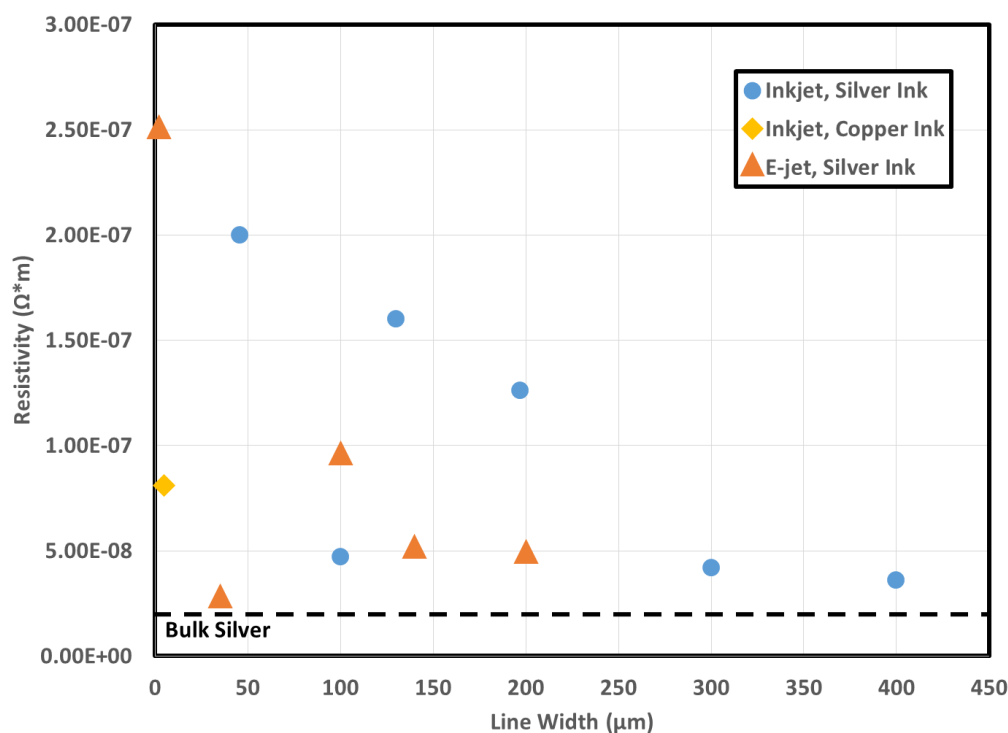


Figure 2.1 Summary of resistivity and width of printed conductive lines reported in the literature.

2.2 Ink Description

The inks used in this study were developed by UT Dots, Inc., a company located in Champaign, Illinois. UT Dots primarily creates nanoparticle inks for use in aerosol jet printing and ink-jet printing [36]. The inks are composed of metallic nanoparticles in organic solvents. For this study, several different silver ink formulations were tested, and results are reported for two of these inks: AgHB and AgDDB. Both contain silver nanoparticles approximately 7-10 nm in diameter. AgHB contains the solvent hexylbenzene, which has a boiling point of 226°C. The silver concentration used for printing was 10%. AgDDB contains the solvent dodecylbenzene, which has a boiling point of 288°C. This ink was printed at both 25% and 50% silver concentrations. While several UT Dots silver inks have previously been successfully demonstrated using inkjet, this chapter shows that conductive AgHB and AgDDB lines can also be printed with E-jet, which allows smaller features to be produced.

2.3 Printing and Annealing Methodology

The inks were printed using 5 μm or 2 μm nozzles at a standoff height of 30 microns from the substrate. The substrate was a silicon wafer coated with a layer of SiO_2 . A pulse width modulated voltage was applied to the nozzle with period, duty cycle, high voltage, and base voltage adjusted to produce a continuous line as narrow as possible. In order to measure resistance, square pads 100 μm per side were printed with centers 1 mm apart and connected by a line as shown in Figure 2.2.

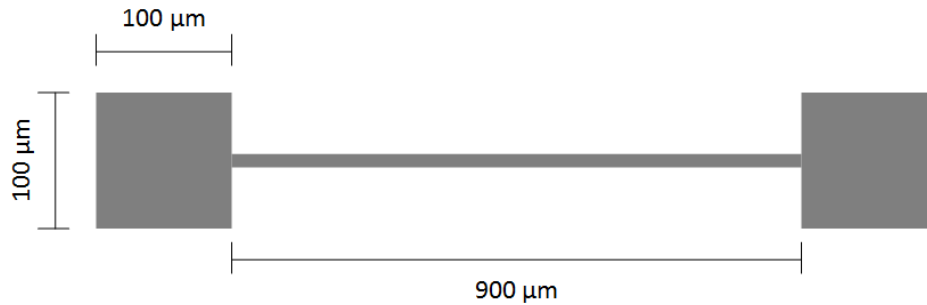


Figure 2.2 Diagram of printing pattern for line with pads.

After printing, it is necessary to anneal silver inks in order to make them conductive. The annealing process consists of multiple steps [37]. First the organic solvent evaporates. Next, the encapsulation around the nanoparticles breaks down. Finally, the silver particles flow together, increasing the grain size of the silver. While there is no formula to determine the appropriate time and temperature at which to anneal the printed ink, some guidelines do apply. In order to eliminate the solvent, the annealing temperature must be greater than its boiling point. It is important that as much solvent as possible be eliminated because any solvent left in the sample will prevent proper silver contact across the entire cross-section of the line and therefore increase its resistance. Generally, for any annealing temperature, resistivity decreases exponentially with time [38]. When the annealing temperature is increased, the rate of decay increases and the final resistivity decreases.

2.4 Challenges

There are several factors which increase the difficulty in printing narrow, conductive lines. Some of these are related to the scaling considerations, while others are inherent in the ink itself.

2.4.1 Nozzle Clogging

The first obstacle to silver ink printing is the tendency under certain circumstances for the nozzle to become clogged. In less severe cases, the clog can be dissolved by submerging the nozzle tip in a solvent such as hexane or toluene. Alternatively, back pressure may be applied to the nozzle to physically push the clog out the tip. In more severe cases, the clog cannot be removed. Ideally, we would like to avoid even temporary occurrences of this issue. The following factors have been observed to cause or increase the likelihood of clogging.

2.4.1.1 Ink Aging

The size of nanoparticles in fresh ink is approximately 7-10 nm. However, over time, nanoparticles begin to agglomerate into larger particles. This can be problematic for two reasons. The first is that larger agglomerated particles may cause clogging either within the capillary or at the tip, particularly since the nozzles used to print the silver ink in this work are typically 5 μm in diameter. This problem can be reduced or eliminated by filtering the ink before adding it to the syringe barrel. The ink was filtered through 400 μm syringe filters before printing. The second reason agglomeration is a problem is that it changes the actual concentration of the ink that is printed. Agglomeration prevents homogenous dispersion of nanoparticles throughout the ink, and therefore when some of the ink is used for printing, its actual concentration is unknown. If the actual concentration is lower than expected, then less silver is deposited during printing, which may decrease line height and increase resistance. Unfortunately, the concentration problem cannot be solved by filtering the ink. Therefore, it is best to print only with ink that does not contain agglomerated particles. From our experience over the course of this study, ink should not be used after approximately three months (or less if particles are visible).

2.4.1.2 Solvent Evaporation at Nozzle Tip

Because the nozzle tip diameter is on the order of microns, even a small amount of solvent evaporation at the tip can be detrimental to the flow of ink. As solvent evaporates, the concentration of silver in the region near the exit of the nozzle increases. This more concentrated ink forms a clog which may partially or completely block the exit and prevent ink from jetting. Therefore, it is best to print with ink containing a solvent with a high boiling point to prevent evaporation of the solvent at the nozzle tip.

2.4.1.3 Silver Concentration

The higher the concentration of silver contained in the ink, the more silver will be deposited in each printing pass. This means that, for an equal number of printing passes, a line made using a higher concentration silver ink will be thicker than a line made using a lower concentration silver ink. Since thicker lines are typically better conductors at this scale, using the highest possible concentration of silver ink should give the lowest resistance with the fewest printing passes. However, if the silver concentration is too high, it may clog the nozzle and be impossible to print at all. Therefore, a balance must be found between printability and amount of silver deposited when it comes to silver concentration. For AgDDB, a 50% Ag w/v concentration was printed. For AgHB, a lower concentration (10% Ag w/v) was required.

2.4.2 Line Continuity

In order for printed silver lines to be conductive, they must be continuous; that is, they must not have any defects causing breaks. Any defects reduce the actual cross-sectional area of the line and will therefore increase its resistance, and major defects that prevent any connection between silver particles at any point in the line will eliminate conduction altogether.

2.4.2.1 Line Breaks during Printing

Discontinuity in the line may occur during printing. If the droplet spacing is too large, the droplets will remain distinct instead of flowing together into a continuous line. Additionally, breaks sometimes occur when printing across pads. One possible reason for these breaks is that the charge deposited when printing the pad has not dissipated, so the electric field in the region

of the pad is not the same as that far from the pad. A higher voltage may be required to print near a pad due to the charge buildup.

2.4.2.2 Line Breaks during Annealing

Even if a continuous line is printed, breaks may occur during the annealing process. If the silver particles are not evenly dispersed (as is the case when ink is not fresh and agglomeration occurs), some sections of the printed line may contain all or mostly solvent rather than silver. When the solvent evaporates during annealing, breaks between silver sections are left. Breaks near pads may also be caused by the reflow of ink that occurs during annealing. As the silver is heated, it tends to flow together. If too much silver is drawn toward the pad, the printed line near the pad will narrow and may even separate as shown in Figure 2.3. This problem can be prevented by switching the printing order: print lines first and then print pads. Alternatively, print pads and lines in a sandwich formation, e.g., print pads first, then print lines, then print another set of pads on top of the first.

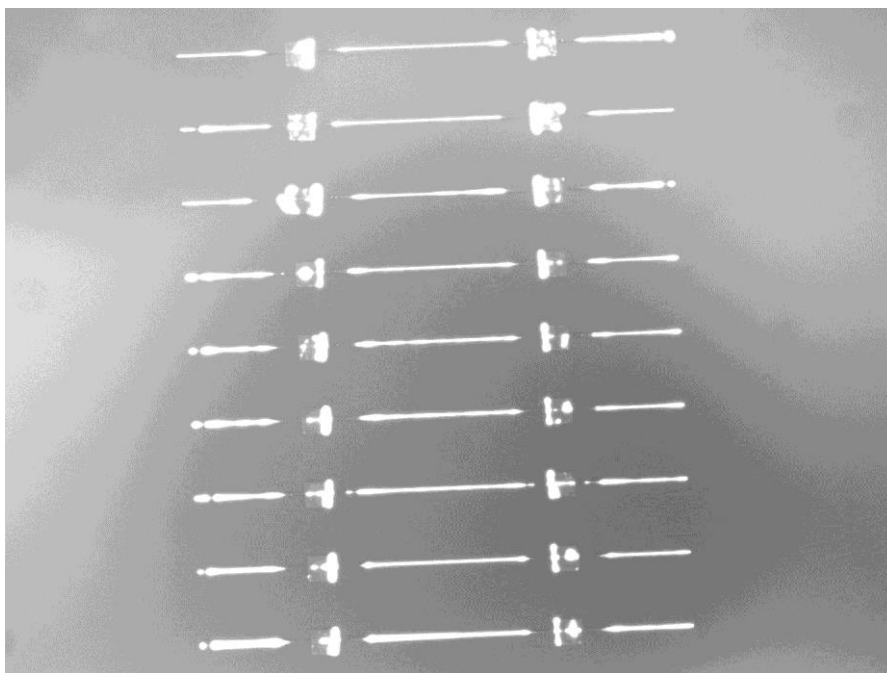


Figure 2.3 Breaks between lines and pads of AgDDB due to reflow of ink during annealing.

2.4.3 Line Thickness

From a large-scale standpoint, the thickness of an approximately rectangular wire should have no effect on its resistivity. A thicker wire should offer less resistance to current, but its geometry is accounted for when calculating resistivity, which is a property of the material. However, for our printed lines, which are less than one micron in thickness, we must consider not only the cross-sectional area, but also the thickness.

It has been observed that the resistivity of thin metallic films is often higher than that of the corresponding bulk materials [39]. This phenomenon is attributed to a scattering effect. If the mean free path of an electron in the bulk metal is greater than half of the thickness of the film, the electron will be scattered by the upper or lower surface of the film. The mean free path of electrons in the thin film will be reduced, and the resistivity of the film will be correspondingly higher than that of the bulk metal. Additionally, scattering may occur at grain boundaries and defect interfaces, and increases with surface roughness of the film [40]. For silver films less than approximately 100 nm in thickness, resistivity is higher than that of bulk silver.

For this reason, it is important to print lines which are at least 100 nm thick in order to approach resistivity values near that of bulk silver. There are several possible methods to achieve such a thickness, two of which are described here.

2.4.3.1 Printing Multiple Passes

One method which may be used to increase the thickness of printed lines and thereby improve their conductivity is to perform multiple printing passes on top of one another. When printing multiple passes, it is important to make sure that the previous pass is at least partially dry. If there is too much solvent still left in the ink when attempting to print a subsequent pass on top, the ink may build up and spread out. This can create wider lines than desired, or worse, deformed edges and bulges. If care is taken to allow partial drying between passes, each printed line should be deposited directly on top of the previous one without increasing the width of the line. The advantage of printing multiple passes is that line thickness may be controlled somewhat arbitrarily because each pass adds approximately the same amount of material. The disadvantage of this method is that it increases the printing time required significantly over printing single-pass lines, particularly if it is necessary to pause between passes to allow the ink to partially dry.

2.4.3.2 Ink-Substrate Interaction

The thickness of a single printing pass on a substrate is largely determined by the degree to which the ink wets the surface. Wetting, which can be quantified by a contact angle between the liquid and solid surfaces, depends on the balance between two forces. Adhesion between the liquid and solid tends to cause the ink to spread and adhere to the surface, and therefore to have a smaller contact angle. Cohesion between molecules of the liquid tends to cause the liquid droplet to remain more spherical, with a smaller liquid-solid interfacial surface area.

When considering wettability of silver inks on various substrates, one should try to find a balance. If the ink does not wet the surface enough, it will not form a continuous line as shown in Figure 2.4 by the AgHB ink printed on a Teflon-coated surface. Although ink may be deposited continuously, the ink will flow on the surface to form bulge and neck regions. Ink flows from the neck regions to the bulges, and eventually the necks break to leave separate droplets rather than a continuous line.

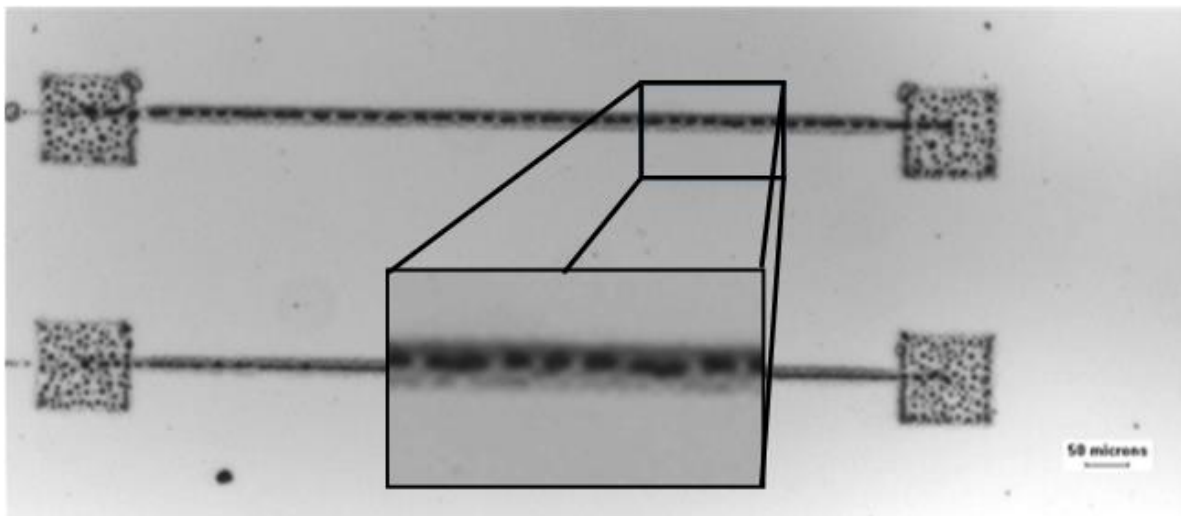


Figure 2.4 AgHB on Teflon showing line breaks due to poor wettability of substrate.

However, if the ink wets the surface too much, the lines will be wide and thin. This creates two problems: first, the lines may be too wide for a desired application; and second, as discussed previously, thin lines do not conduct electricity as well as thicker lines. The degree of wettability must therefore be high enough so as to form continuous lines, but low enough that the lines are narrow and thick.

All of the samples discussed in the results section of this chapter were printed on SiO₂. A clean SiO₂ surface allows a relatively high degree of wetting by many organic solvents due to its high surface energy [41] and is therefore a good choice for a substrate to be used in combination with the inks from UT Dots.

2.4.4 Coffee Ring Effect

2.4.4.1 Explanation

When first printed, silver ink lines have a convex surface with the center higher than the edges. After annealing, however, the line often has thicker edges with a “dip” in the center as seen in Figure 2.5.

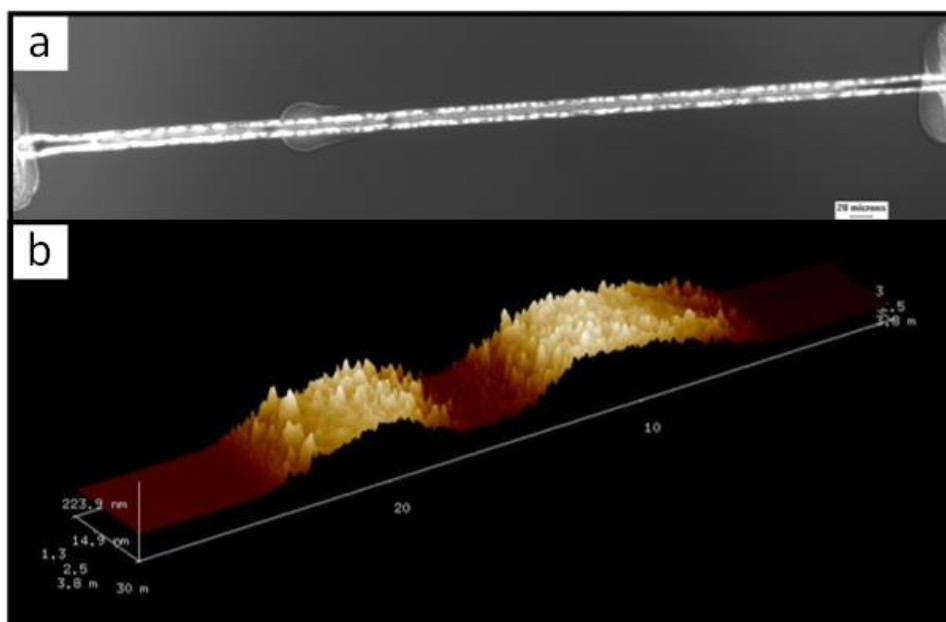


Figure 2.5 AgHB line exhibiting coffee ring effect in (a) optical microscope image and (b) AFM height measurement plot.

This can be explained by a phenomenon known as the coffee ring effect. When a line of silver ink is printed, some of the solvent begins to evaporate. Since the contact lines on the outer edges of the printed line are pinned (that is, the printed line cannot become narrower), some of the ink from the center must flow toward the edges to replace the evaporated solvent [42]. As ink flows outward, more silver particles are carried toward the edges of the printed line. During

annealing, this process continues. When all the solvent is removed, the cross-section of the remaining silver has two peaks at the edges with a valley in the center. This process is illustrated in Figure 2.6.

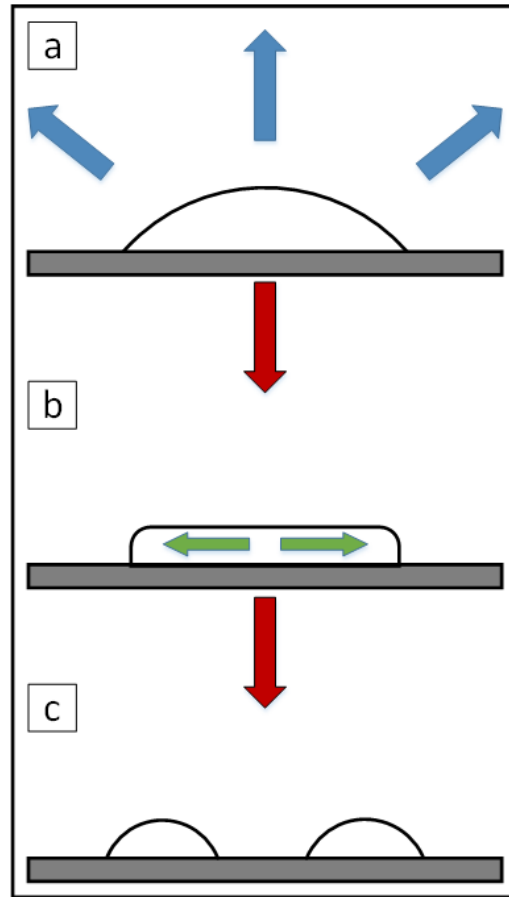


Figure 2.6 Illustration of the coffee ring effect: (a) solvent evaporation, (b) ink flow to replace lost solvent at edges, (c) buildup of solute at edges as solvent evaporates.

2.4.4.2 Methods to Reduce the Effect

Aside from aesthetic considerations, the coffee ring effect is undesirable for printed silver lines because it increases their [43]. When most of the silver is contained in the ridges at the outer edges of the printed line, the center portion of the line does not provide a conductive pathway. The thin layer of silver left in the center often contains cracks or defects produced during annealing. There have been a few methods proposed to reduce the coffee ring effect and to create more uniform printed lines. Two of these were attempted for E-jet printed silver lines.

2.4.4.2.1 Marangoni Flow

In order to counteract the outward flow of ink that carries and deposits silver nanoparticles at the edges of a printed line, another type of flow, called Marangoni flow, can be induced to recirculate ink back to the center. Marangoni flow occurs due to a difference in surface tension. A liquid is pulled from areas of low surface tension toward areas of high surface tension. In the case of printed silver ink, this effect can be created by the addition of a solvent with a higher boiling point and lower surface tension than that of the original solvent. For example, Kim et. al. [43] printed a water-based ink and added ethylene glycol. The water, which has a lower boiling point, evaporated faster at the contact line and drew ink outward. As the water evaporated, the concentration of ethylene glycol, which has a lower surface tension, increased toward the edges. Therefore, the ink also flowed toward the center, which had a relatively higher surface tension than the edges. The overall effect was a recirculation from the center to the edges along the substrate and from the edges back to the center across the surface of the ink, which created a more uniform surface than with water alone.

This method was attempted using an ink containing two solvents. The first solvent was proprietary and designated as “C”. The added solvent was Eucalyptol, which has a higher boiling point and lower surface tension than does “C”. Unfortunately, this ink formulation caused undissolvable clogging in the nozzle and was therefore unable to provide useful results.

Adding a solvent to generate Marangoni flow is still a potentially viable method to reduce the coffee ring effect, but it will require further study. An investigation as to why these particular solvents caused clogging is beyond the scope of this work, but could lend insight into ink properties which create Marangoni flow without causing the nozzle to clog during printing.

2.4.4.2.2 Cold Printing

A second method which has previously been used by Soltman and Subramanian to eliminate the coffee ring effect is to reduce the temperature of the substrate during printing [44]. Because the amount of liquid at the edges of a drop is smaller, heat is transferred from the substrate to the edge of the drop or vice versa more quickly than from the substrate to the center of the drop. When the substrate is heated, the edges of the drop heat up more quickly than does the center, and therefore evaporation occurs at a faster rate near the edges of the drop, increasing

the coffee ring effect. When the substrate is cooled, the opposite effect occurs: heat is transferred from the droplet to the substrate faster at the edges than at the center of the drop, slowing evaporation at the edges. This reduces the flow of ink toward the droplet edges, so less solute is deposited there.

This method was attempted in two ways: first, a portable air conditioning unit was used to cool a desktop E-jet system inside an environmental chamber to 14°C. Second, a Peltier cooler was used to cool the substrate to -10°C. In both cases, the nozzle clogged, possibly due to aggregation of the silver nanoparticles. Ideally, the substrate would be cooled without cooling the ink inside the nozzle. However, due to the close proximity of the nozzle tip to the substrate, both nozzle and substrate were impacted by both of our cooling methods.

In the future, attempts to reduce the coffee ring effect by cold printing should avoid cooling the ink inside the nozzle. One way to accomplish this would be to place a Peltier cooler directly under the substrate. A new substrate mount should be designed for this purpose.

2.5 Results

2.5.1 Optical Microscope Images of Printed Lines

Images of each of the samples were taken with an optical microscope in order to assess the width and quality of the lines. Figure 2.5(a), shown in section 2.4.4.1, shows an image of a 30-pass AgHB line after annealing. This line is approximately 20 μm wide. The edges of the line are fairly straight, but they are much brighter than the center, indicating that the edges contain more silver than does the center. As previously mentioned, this example of the coffee ring effect increases the resistance of the line.

Figure 2.7 shows a 20-pass AgHB line after annealing. Once again, the coffee ring effect is visible. The edges of this line are slightly wavy, and the width is about 20 μm with some thinning effect near the pads as discussed previously.

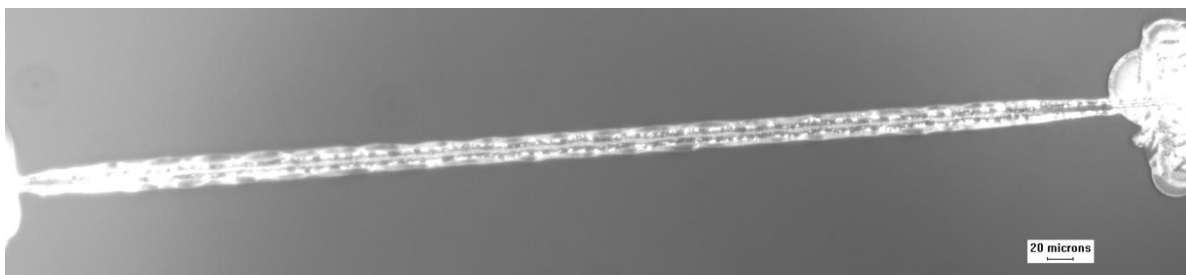


Figure 2.7 Optical microscope image of 20-pass AgHB line (10% w/v Ag) printed with 5 μm nozzle after annealing.

Figure 2.8 and Figure 2.9 show 10-pass and 20-pass samples of AgDDB ink with 25% w/v Ag. The lines were printed with 5 μm nozzles. Unlike the AgHB lines, these samples do not show signs of the coffee ring effect. They appear smoother, but the line edges are slightly wavy. The 20-pass line appears brighter than the 10-pass line because it contains more silver. Both lines are approximately 9-10 μm in width.

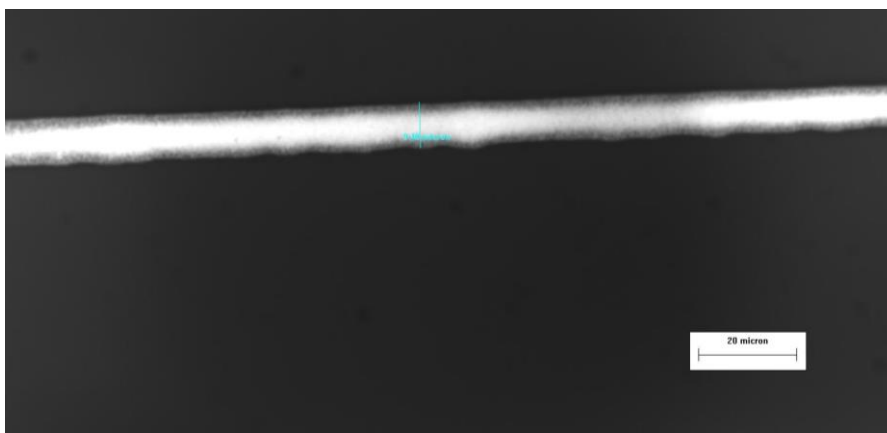


Figure 2.8 Optical microscope image of 10-pass AgDDB line (25% w/v Ag) printed with 5 μm nozzle after annealing.

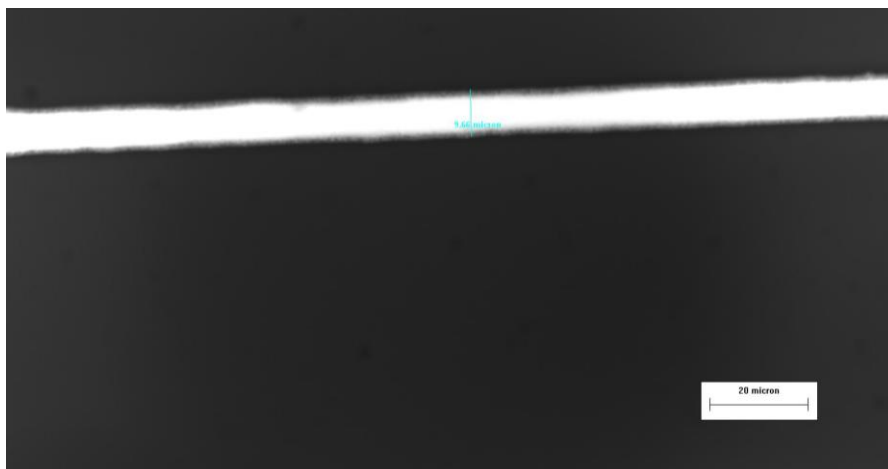


Figure 2.9 Optical microscope image of 20-pass AgDDB line (25% w/v Ag) printed with 5 μm nozzle after annealing.

Figure 2.10 shows a 20-pass line of AgDDB ink with 50% w/v Ag. This sample was printed using a 5 μm nozzle. It appears similar to the 20-pass AgDDB line with a lower concentration of silver. The width of this line is also approximately 10 μm . It is mostly smooth and straight, with some waviness near the right pad.



Figure 2.10 Optical microscope image of 20-pass AgDDB line (50% w/v Ag) printed with 5 μm nozzle after annealing.

In Figure 2.11, the same ink (AgDDB with 50% w/v Ag) was used with a 2 μm nozzle to print narrower lines. With this smaller nozzle, the AgDDB lines are 3-4 μm in width. No coffee ring effect is visible, but the edges of the line are relatively wavy compared to its overall width.

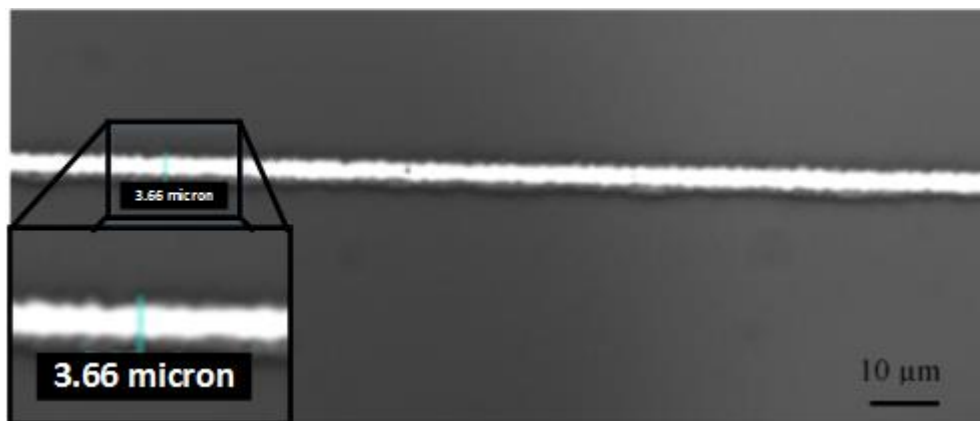


Figure 2.11 Optical microscope image of 25-pass AgDDB line (50% w/v Ag) printed with 2 μm nozzle after annealing.

2.5.2 Resistance Measurement

Resistance was measured by touching probe tips to the printed pads and holding one probe at 0V while sweeping the voltage of the other probe from a negative to a positive potential. The current was measured simultaneously. The resistance was determined by calculating the slope of the voltage vs. current plot. Data for both 20-pass and 30-pass AgHB lines is given in Figure 2.12. In this case, the resistance of the 20-pass line is 131 Ω , while the resistance of the 30-pass line is 43 Ω .

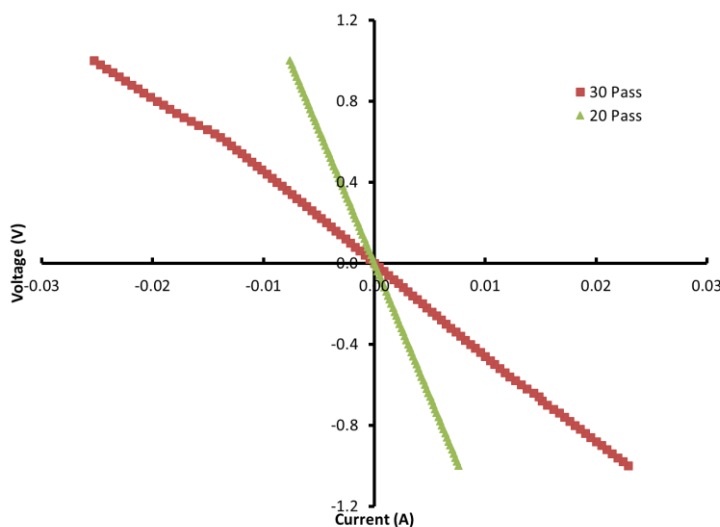


Figure 2.12 Current measurements during voltage sweep for 20- and 30-pass AgHB (10% w/v Ag) lines printed with 5 μm nozzle used to calculate resistance.

Figure 2.13 shows the current measurements during a voltage sweep for both 10-pass and 20-pass lines of AgDDB with 25% w/v Ag. The resistance for the 10-pass line is 735 Ω , while the resistance for the 20-pass line is 76 Ω .

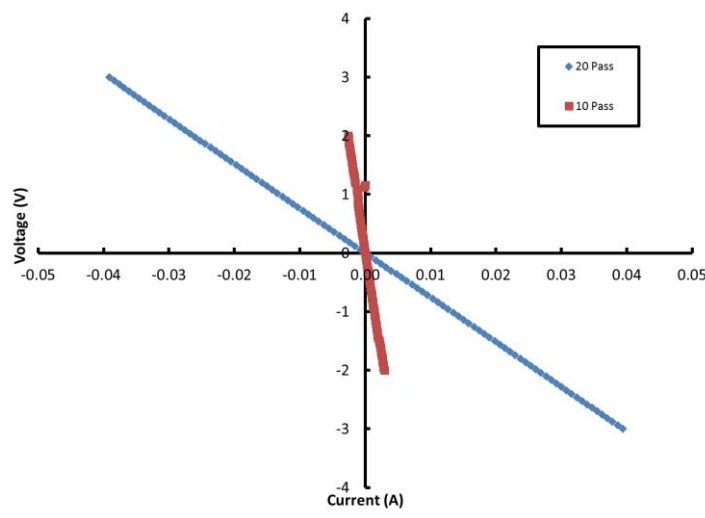


Figure 2.13 Current measurements during voltage sweep for 10- and 20-pass AgDDB (25% w/v Ag) lines printed with 5 μm nozzle used to calculate resistance.

Figure 2.14 shows the current measurement during a voltage sweep for a 20-pass AgDDB line with 50% w/v Ag. The resistance for this line was 39 Ω .

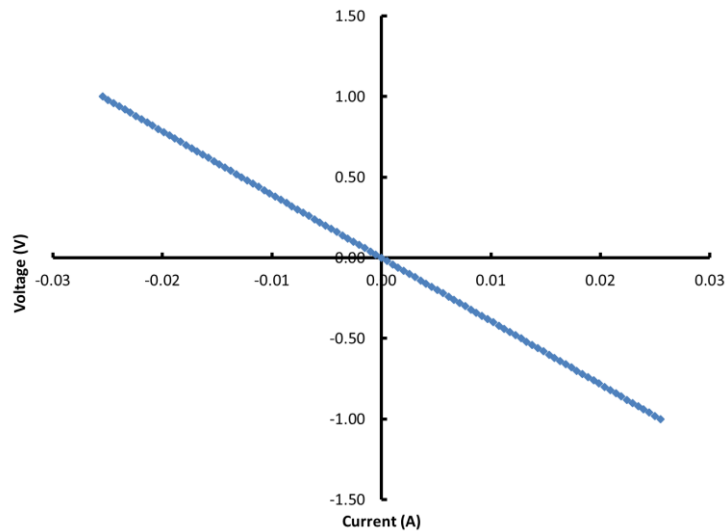


Figure 2.14 Current measurements during voltage sweep for 20-pass AgDDB (50% w/v Ag) lines printed with 5 μm nozzle used to calculate resistance.

Figure 2.15 shows the current vs. voltage plot for the 25-pass AgDDB sample at 50% w/v Ag printed using a 2 μm nozzle. The resistance for this sample was 352 Ω .

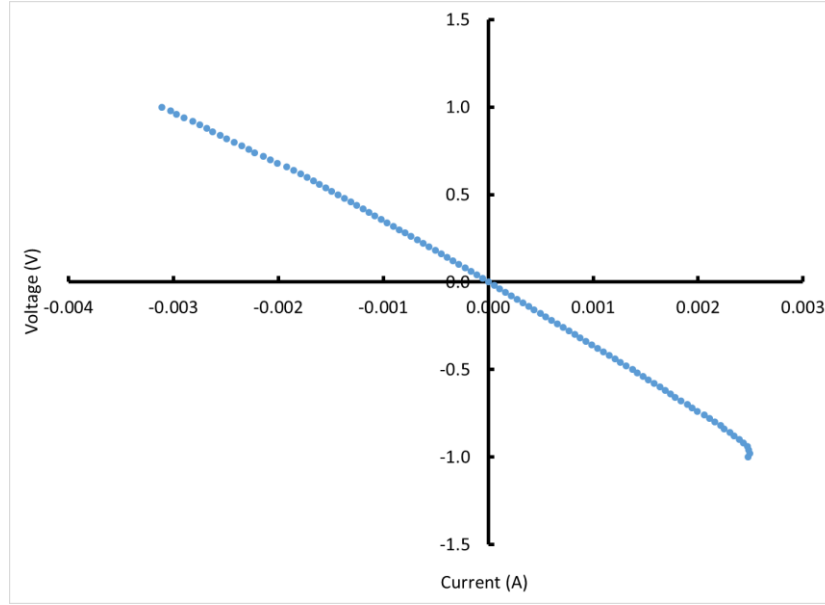


Figure 2.15 Current measurements during voltage sweep for 25-pass AgDDB (50% w/v Ag) lines printed with 2 μm nozzle used to calculate resistance.

From these results, it is clear that the resistance decreases as the number of printing passes increases and as the nozzle size increases. However, in order to characterize various inks, we need a measure of performance which is not dependent on the geometry of the printed lines. In the following sections, we will calculate the resistivities of the samples and use those values to compare the performance of the inks.

2.5.3 Height Measurement and Cross-Sectional Area Calculation

An atomic force microscope was used to measure the height of the printed line. Sixty-four scans of length 30 μm were performed with 256 measurements taken per scan. Previously, an example of height scan data for a 30-pass AgHB line was shown in Figure 2.5(b) in section 2.4.4.1.

The raw data were adjusted so that the background was flat, i.e., that the height readings on either side of the line were approximately zero as shown in Figure 2.16. Note that this figure shows only one line scan out of the 64 total scans taken for this sample. This plot illustrates the coffee-ring effect seen in all AgHB samples. The cross-sectional area under the curve was

calculated by finding the average of all the height measurements in the scan and multiplying by the width of the line. The average height for this line is approximately 140 nm, giving a cross-sectional area of approximately $2.8 \times 10^{-12} \text{ m}^2$.

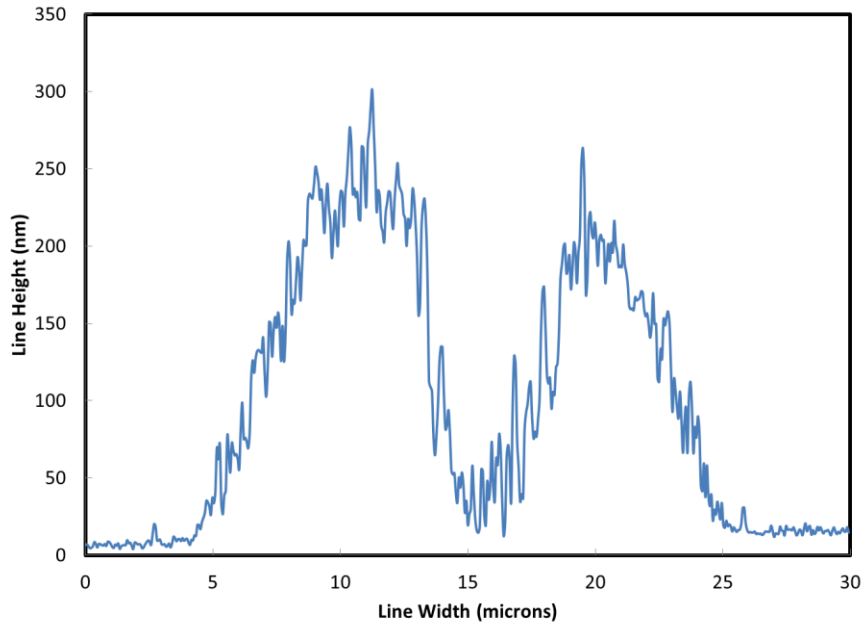


Figure 2.16 Adjusted height measurements for a single line scan of 30-pass AgHB.

The same process was conducted for the 20-pass AgHB line as well as the AgDDB samples. For both AgHB samples, the edges of the lines are on the order of hundreds of nanometers, but the center of the line is less than 50 nm.

Figure 2.17 shows the AFM height data for the 20-pass AgHB line. This line has a relatively large surface roughness compared to its height, which may negatively impact its conductivity. The average height of this line is approximately 100 nm, which gives an approximate cross-sectional area of $2.0 \times 10^{-12} \text{ m}^2$.

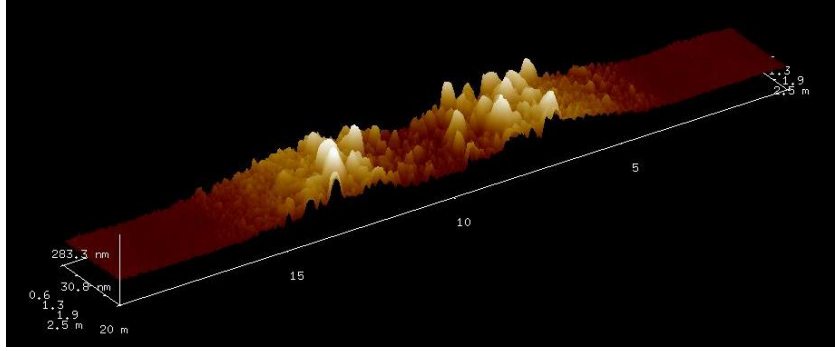


Figure 2.17 AFM height measurements for 20-pass AgHB (10% w/v Ag) printed with 5 micron nozzle.

Figure 2.18 shows the AFM height data for the 20-pass AgDDB line printed using a 5 μm nozzle. This line has a few very large grains near the center which may increase the resistivity. However, the coffee ring effect is not visible with this ink. The average height of this line is approximately 178 nm, which gives an approximate cross-sectional area of $1.8 \times 10^{-12} \text{ m}^2$.

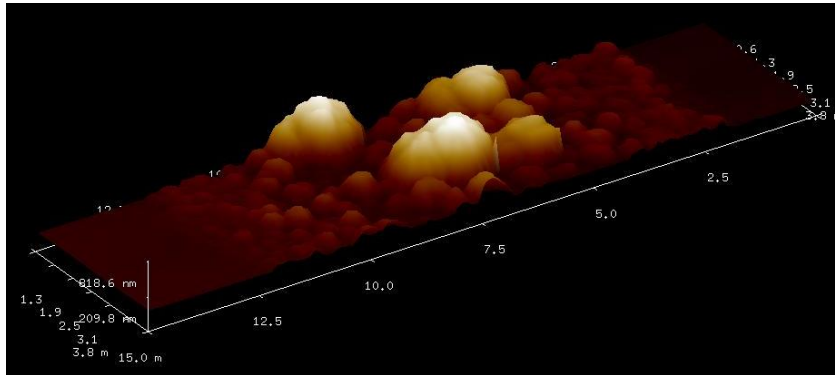


Figure 2.18 AFM height measurements for 20-pass AgHB (10% w/v Ag) printed with 5 micron nozzle.

Figure 2.19 shows AFM height measurements for the AgDDB sample printed with a 2 μm nozzle. From these images, AgDDB does not suffer from the coffee ring effect as did AgHB. Instead, the center of the line is taller than the edges. A possible explanation for the wider base is that the initial pass spread out on the SiO_2 surface due to poor adhesion, while subsequent passes remained in place as they were printed because the ink adheres well to itself. The average height of this line is approximately 90 nm, giving it a cross-sectional area of approximately $3.6 \times 10^{-13} \text{ m}^2$.

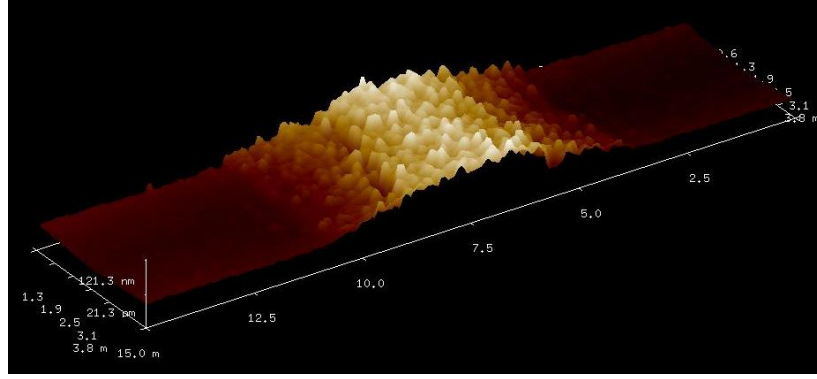


Figure 2.19 AFM height measurements for 25-pass AgDDB (50% w/v Ag) printed with 2 micron nozzle.

2.5.4 Resistivity Calculation

The quality of printed conductive lines is determined primarily by their resistivity, which is a calculated parameter given by Eq. 2.1 that takes into account both measured resistance and size of the line. Resistivity is a property which describes the ability of a material to resist carrying an electric current. Lower values of resistivity are better, with the lower limit determined by the resistivity of the bulk metal. While resistance depends on the geometry of the material, resistivity should be the same for any given configuration, making it an appropriate choice for comparing the performance of conductive materials.

$$\rho = R \frac{A}{l} \quad (2.1)$$

In Eq. 2.1, R represents the resistance of the sample as calculated using the slope of the current vs. voltage line. A is the cross-sectional area of the sample as calculated from AFM height measurements. l is the length of the sample. For all of the samples except those printed with the 2 μm nozzle, the distance between the pads is 0.9 mm. For the samples printed with the 2 μm nozzle, the distance between pads is 0.7 mm.

A summary of the resistance, cross-sectional area, length, and calculated resistivity of all AgHB and AgDDB samples is presented in Table 2.1. The lowest resistivity was achieved with the 20-pass line of AgDDB with 50% Ag printed with a 5 μm nozzle, while the narrowest line was printed with 25 passes of AgDDB with 50% Ag using a 2 μm nozzle.

In general, the AgHB samples have a higher resistivity than the AgDDB samples. One reason this could occur is that, due to the coffee ring effect, the AgHB lines suffer more from the scattering effect discussed previously. Figure 2.16 above illustrates that across most of the line width, the height is less than 150 nm. For the AgDDB lines, there is no coffee ring effect, so the resistivity is lower.

Table 2.1 Summary of resistance, geometry, and resistivity of silver lines printed with E-jet.

Ink Type	Ag Concentration	Nozzle Size	Number of Passes	Resistance	Cross-Sectional Area	Length	Resistivity
	% w/v	μm		Ω	m^2	mm	$\Omega \cdot \text{m}$
AgHB	10	5	20	131	2.0×10^{-12}	0.9	2.9×10^{-7}
			30	43	2.8×10^{-12}	0.9	1.3×10^{-7}
AgDDB	25	5	10	735		0.9	
			20	76		0.9	
	50	5	20	39	1.8×10^{-12}	0.9	7.8×10^{-8}
	50	2	25	352	3.6×10^{-13}	0.7	1.8×10^{-7}

2.5.5 Analysis

Ideally, all of the silver nanoparticle inks should produce lines which, after annealing, have a resistivity the same as that of bulk silver regardless of sample geometry. The resistivity of bulk silver is $1.59 \times 10^{-8} \Omega \cdot \text{m}$. The resistivity values for the printed lines are approximately ten times that of bulk silver.

There are several possible reasons why the printed lines have higher calculated resistivity values. First, the printed lines may contain some defects which occur during either printing or annealing including scratches, necking, and wavy edges. These are not accounted for in the cross-sectional area calculation, which is based on measuring the width of the line at several points and taking the average height over a relatively small portion of the sample. The resistivity calculation is based on a constant cross-sectional area for the entire length of the sample, which in practice is unrealistic. Defects cause the cross-sectional area at some points to be smaller than the nominal area. This causes the calculated resistivity value to be higher than the actual resistivity.

Additionally, as mentioned previously, scattering of electrons may occur both at the upper and lower surfaces of the line as well as at grain boundary interfaces. The printed lines

shown in this work have a thickness which is near the threshold for surface scattering of electrons creating an impact on resistivity. Annealing should increase the grain size of the silver and reduce grain boundary scattering of electrons, but this may still have an impact on the measured resistance of the lines.

Based on both ease of printing and resistivity, AgDDB appears to be the superior choice as compared to AgHB for E-jet printing applications. While occasional clogging did occur with both solvents, it was more frequent for AgHB. We were able to print with a higher silver concentration using the AgDDB ink, which is important not only because more silver is likely to be deposited with each printing pass, but also because there is less solvent to be removed during the annealing process. Additionally, AgDDB can be printed using a nozzle with a tip as small as 2 μm , while AgHB required at least a 5 μm nozzle. This facilitated the printing of narrower lines using AgDDB—as small as 3-4 μm . Finally, the lowest resistivity value was achieved with AgDDB, likely a consequence of the ability to print at a higher silver concentration. There is a tradeoff in regard to line width and resistivity: the lowest resistivity was achieved with a 5 μm nozzle, which produced a 10 μm line. The determination of which nozzle size to use should be made according to the resistivity and line size requirements of the application.

2.6 Conclusions and Future Work

In this chapter, we have demonstrated E-jet printing of 4-20 μm lines of silver nanoparticle ink. These lines are narrower than the lower limit of capability of other additive manufacturing methods such as inkjet. As a comparison to the previous results reported in the literature, here we reproduce Figure 2.1 with the results from the current work added as Figure 2.20.

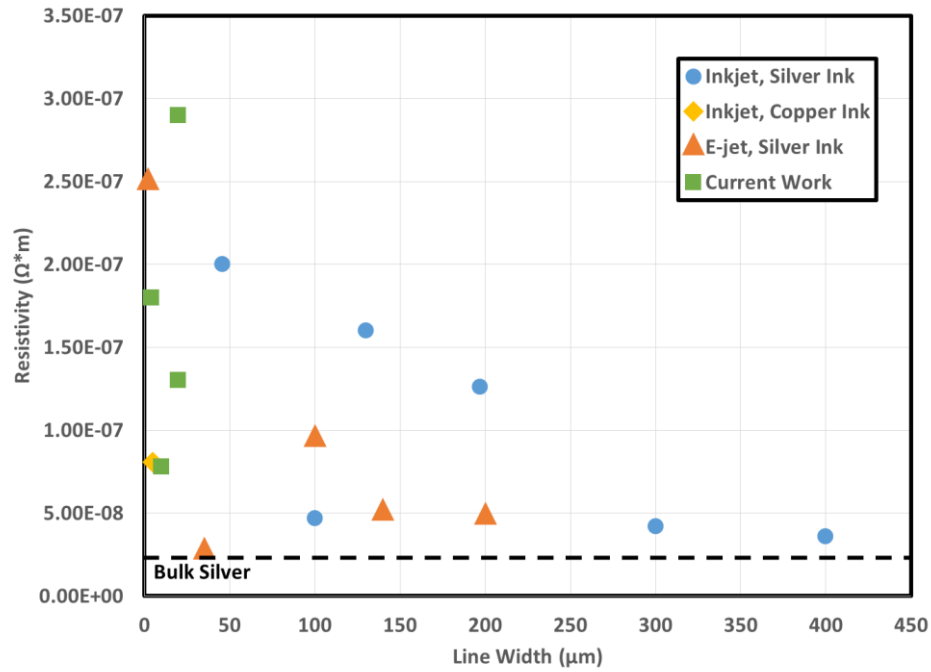


Figure 2.20 Comparison of resistivity and width of printed conductive lines reported in the literature to lines printed in the current work.

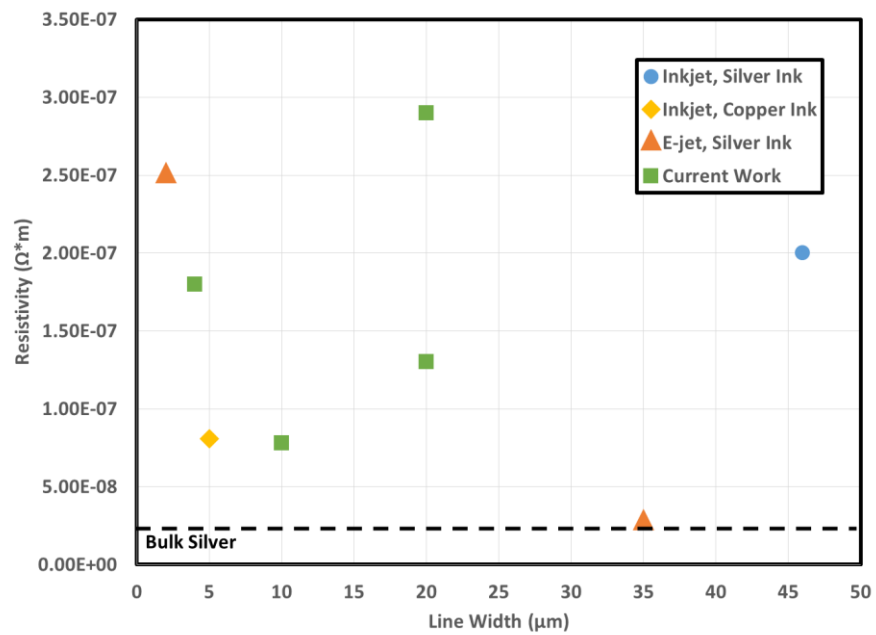


Figure 2.21 Comparison of resistivity and width of printed conductive lines reported in the literature to lines printed in the current work (detail view).

Several printing challenges were described along with methods to avoid or reduce these problems. The performance of the printed lines was assessed by measuring their resistance and geometry and calculating their resistivity. The resistivity achieved in this study is a few times that of bulk silver, which is acceptable for many potential applications.

Now that narrow, conductive printed lines have been demonstrated using the E-jet, the next step is to incorporate these printed lines into small-scale electronic devices. Recently, there has been an interest in the production of small-scale transistors via additive manufacturing methods. All transistors include three basic components: a semiconductor, an insulator, and conducting source, drain, and gate electrodes. Inkjet printers have been used to print both complete transistors and portions of transistors, but they are fundamentally size-limited due to the size of the inkjet nozzle. The inks demonstrated in this chapter can be used to print conductive electrodes on a smaller scale which may be incorporated with semiconducting and insulating layers produced with other manufacturing methods. Alternatively, if semiconducting and insulating ink printing is also tuned for E-jet, an entire transistor may be printed using this method. Other potential applications of printing conductive inks include RFID antennae, microscale capacitors, and interconnects for circuits of various types.

Additionally, in order for E-jet printing of electronics to be commercially viable, the printing process should be improved in terms of speed and repeatability. The speed of manufacturing may be improved by incorporating multiple nozzles into a single print head, thus allowing multiple device interconnects to be printed simultaneously [45]. The process could also be tuned so that each printing pass requires less time to complete. By selecting substrates which have relatively low wettability for the ink under consideration, fewer printing passes would be required to achieve the same height, significantly reducing printing time. The ability to attain a printing time of 1 ft²/min or less would match commercial inkjet printing speeds [46]. In terms of repeatability, further study with a large number of samples will allow the variation in width, height, and resistivity of printed lines to be quantified. Environmental factors such as humidity should be investigated to determine their effects, if any, on both the printing process and the characteristics of the printed lines. The annealing procedure should be tuned for each ink to find the appropriate time and temperature values to achieve the best possible conductivity.

Chapter 3

Single Drop Modeling and Validation

3.1 E-Jet Modeling Background

An efficient manufacturing system must produce predictable and repeatable results. In order to predict and control a system, we must first be able to understand it. Developing an understanding of the underlying physical aspects which govern the behavior of a system and creating models to describe its behavior allows us to manipulate its parameters to improve the process. A good example of this concept is the study of the effects of various types of pressure waves used to produce droplets in inkjet printing. Modeling efforts in this area led to the development of a standard pulse shaping approach which is used to eliminate unwanted satellite droplets and improve the quality of printing [47].

Several authors have studied and modeled particular aspects of the jetting process for E-jet. Because the jetting process is complex and not completely understood, some of these models contradict one another, and most do not attempt to give a complete description of jetting. Modeling efforts have focused on, for example, droplet size and charge, frequency of jetting, and the formation of the Taylor cone.

Marginean et. al. explain the process of jet formation [48]. They describe a four-phase cycle of liquid accumulation, cone formation, jet ejection, and relaxation which is observed with high-speed imaging. However, they do not mention any observation of a multiple-drop pattern.

Aksay et. al. develop a set of scaling laws for the frequency of pulsation of a jet observed due to depletion and refilling of the cone tip [49].

Deng and Gomez break down cone and jet formation into several steps and give laws to determine the time required for each step [50].

Basaran et. al. have created a finite-element model based on the Navier-Stokes equation which leads to a scaling model for drop size based on ink properties and system geometry [17]. The same researchers also give a scaling law for the charge on a droplet [51].

The models described above are useful in predicting or explaining certain aspects of E-jet drop formation. However, as will be shown later in this chapter, we have observed that jetting for certain inks occurs in characteristic cycles which include multiple drops per cycle. There remains a need for a model which can describe both the trajectory of a jet from the nozzle to the substrate and explain the multi-drop cycle observed under some conditions.

3.2 Development of Jetting Model Structure

Previous models for E-jet printing have been “white-box” models; they were developed based on a consideration of first principles. While white-box modeling has given very detailed and accurate predictions for specific aspects of jetting, a white-box model which is able to describe a full jetting cycle would be very complex. The time and computational cost required in not only developing such a model, but also applying it to various applications, may be prohibitive.

As a solution, we will make a compromise between desired simplicity and accuracy in the model representation of printing. We will make some assumption about the structure of the model which are based on knowledge of the physics behind jetting. This makes our identification different than black-box system identification, for which there is no prior knowledge about the system. However, the result is less complex than a true white-box model which considers all physical aspects of the system. Therefore, it falls in the category of “gray-box” models [52].

The goal of this research is to produce a relatively simple model for E-jet ink ejection which provides insight into the physical phenomenon as well as allowing improvements to the jetting process to be made. We do not attempt to perfectly represent every detail of the process, but rather to give a more complete picture of the entire cycle than has previously been developed. The approach taken here is to develop a representation of a jet based on a charged mass-spring-damper analogy and compare the jet tip position given by the model to high-speed

video data collected during ink ejection. In this chapter, we focus on a single drop from nozzle to substrate. In the next chapter, we explain a full jetting cycle with multiple drops.

3.2.1 Mass-Spring-Damper System

In the 1970s and 1980s, various researchers observed chaotic behavior in water droplets falling from a leaky faucet. Shaw et. al. [53] described this phenomenon using a simplified “mass on a spring” model as given in Eq. 3.1.

$$\frac{d(mv)}{dt} = mg - ky - bv \quad (3.1)$$

This height y of the droplet in this model depends on the constant parameters g , k , and b as well as the rate of change of m . While m and g correspond to the mass of the droplet and the gravitational acceleration, b and k are not defined in terms of any physical properties of the system. Instead, the model as a whole simply describes the oscillatory behavior of the height of a droplet. Note that the rate of change of the mass is based on the flow rate of liquid to the faucet, but a discrete drop in mass occurs whenever a droplet breaks off. The condition for a droplet to break away is that it reaches a certain predefined height. Other researchers have taken this modeling approach and made additions or corrections to more closely approximate the actual behavior of liquid dripping [54], [55], [56].

Ejection of ink from a nozzle using the E-jet can be modeled in a similar manner. We treat the jet in two parts. The tip of the jet is expected to contain the majority of the mass and charge, and is treated as a point mass and point charge for the sake of simplicity. The tail of the jet is a narrower filament connecting the jet tip to the nozzle. It is treated as a spring and damper in parallel. The spring and damping constants can be treated as arbitrary parameters. Figure 3.1 illustrates the mass-spring-damper model of the jet.

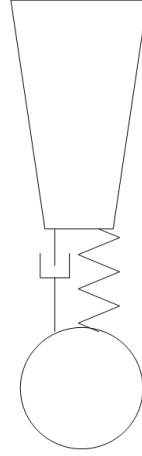


Figure 3.1 Diagram of jet modeled as a mass connected to the nozzle by a spring and damper.

There are three forces acting on the jet tip under consideration. The first two are a spring force and a damping force produced by the ink forming the tail of the jet, which tend to pull the jet tip back toward the nozzle during ejection. The third force is caused by the charged jet tip being acted on by an electric field created by the application of a high voltage to the nozzle while the substrate below is grounded. The electrical force tends to pull the charged jet tip toward the grounded substrate. A free-body diagram showing these three forces is given in Figure 3.2. The equation of motion for this system is given in Eq. 3.3.

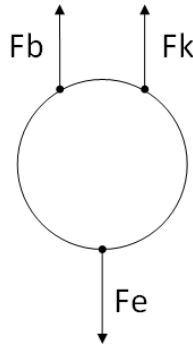


Figure 3.2 Free-body diagram of the forces acting on the jet tip.

$$m\ddot{z} = F_k + F_b + F_e \quad (3.2)$$

$$m\ddot{z} = kz + b\dot{z} + F_e \quad (3.3)$$

One distinction between E-jet ink ejection (jetting) and the dripping models described previously is that, at least for the ink type and system dimensions studied, the jet does not break up to form a free-falling droplet. Instead, the jet extends all the way to the substrate, the tip breaks off and remains on the substrate, and the tail retracts back toward the nozzle. Therefore, the critical height for droplet breakoff used in this model is the height of the substrate. Our approach to the breakoff height of a droplet from the jet tail is based on observations from high-speed video discussed later in this chapter. For other inks, jet breakup may occur mid-flight, in which case it is important to determine the height at which the breakup occurs. The same general approach to modeling would still apply to such a system, but the spring and damping forces caused by the jet will go to zero when the droplet breaks away.

3.2.2 Electric Field

Ink is ejected in the form of a droplet connected to the nozzle. For this model, charge is assumed to be concentrated at the tip of the jet and is treated as a point charge.

With this approximation in mind, we consider the effect of the grounded substrate. A well-known method in electrostatics for representing a ground plane called the “method of image charges” allows the plane to be replaced by a set of charges which create an equivalent electric field. Using this method, for any charge placed on one side of the ground plane, an equal but opposite charge is placed on the other side. The distance from the first charge to the ground plane is equal to the distance from the second “image” charge to the plane. The total electric field can then be determined by summing the contributions from both real and “image” charges.

In the case of a single nozzle held at a fixed voltage producing a charged jet tip or droplet above a grounded substrate, in which we have approximated the droplet as a positive point charge, we will replace the grounded substrate with a negative point charge. The image charge is the mirror of the droplet charge, and therefore it will mirror the movements of the droplet. It will have a charge equal and opposite to the droplet charge. Figure 3.3 illustrates the representation of a jet tip and a grounded substrate using the image charge method.

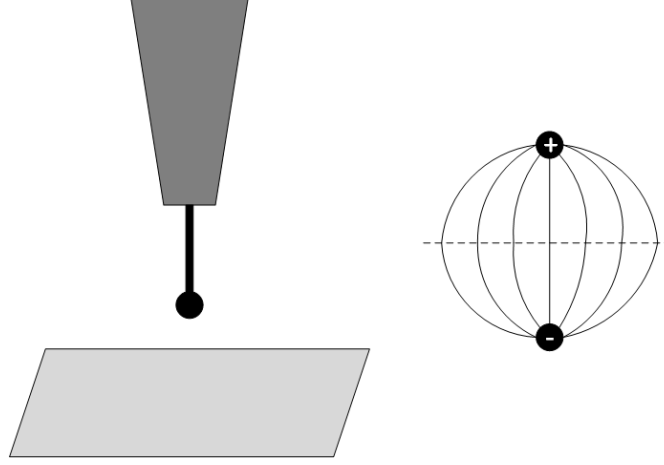


Figure 3.3 Method of image charges used to describe the electrical field due to a jet produced by a single nozzle above a grounded substrate.

Extending this idea to two or more nozzles requires the addition of point charges representing the jet tips (if any) from other nozzle(s) as well as corresponding image charges as shown in Figure 3.4.

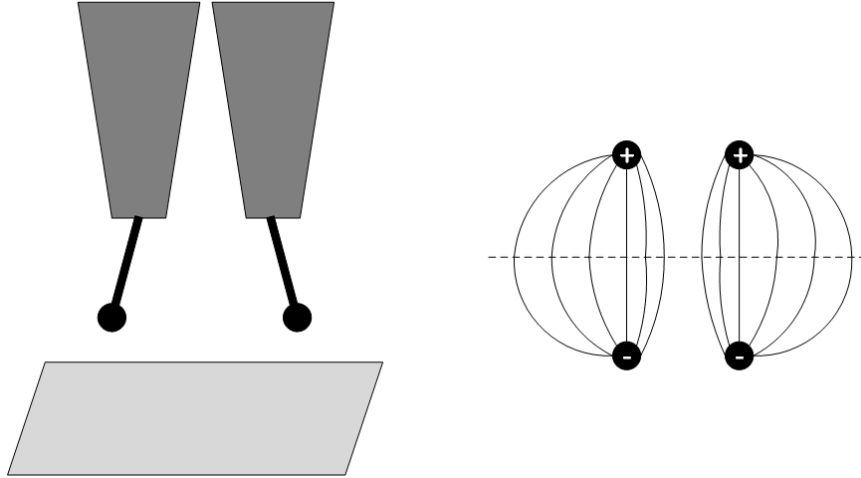


Figure 3.4 Method of image charges used to describe the electrical field due to jets produced by multiple nozzles above a grounded substrate.

Eq. 3.4 describes the electric force on a jet tip produced by a single nozzle, where q is the charge on the jet tip, m is the mass of the jet tip, z is the distance from the jet tip to the nozzle, z_s is the distance from the substrate to the nozzle, and c is Coulomb's constant.

$$F_e = \frac{cq^2}{4m(z_s - z)^2} \quad (3.4)$$

3.2.3 Assumptions and Approximations

As explained above, the second-order model we have developed is a gray-box model, so we have intentionally sacrificed a certain level of accuracy in order to maintain simplicity. For this reason, our system parameters do not directly correspond to single physical properties, but are instead a combination of properties.

The charge on jet is approximated as a point charge contained in the tip of the jet. The electric field model is based entirely on this point charge and its interaction with the grounded substrate. Any contribution to the electric field due to the nozzle or the jet tail after the jet begins its trajectory are neglected.

As previously mentioned, the mass of the jet is treated as a point charge located at the tip of the jet. While the tail does contain some mass, it is assumed that this mass is negligible compared to the jet tip due to the small diameter of the filament that forms the tail.

The spring-and-damper representation of the tail is based on the idea that the tail is elastically stretched. During jetting, it is assumed that there is no ink flow from the nozzle. Instead, the ink which was contained in the meniscus before jetting makes up the jet tip and tail. This means that the mass is considered constant during a drop.

There are many forces on the jet which are not explicitly considered in this model, including surface tension, viscous forces, gravity, and drag. The forces which represent a significant contribution are represented collectively by the spring and damping forces in the model.

3.3 Imaging with High-Speed Camera

Because the duration of jetting is short (for NOA 74, less than 600 μs), a standard video camera recording at 30 frames per second or fewer will not capture the event. Two different imaging methods were used in an attempt to capture enough data to compare to the model previously described.

3.3.1 Strobe Imaging

The first method used to capture the jetting process was strobe imaging. The idea behind strobe imaging is to flash a light very briefly at the same time the event to be captured occurs

while recording with a video camera. When the event occurs repeatedly, as with jetting, the frequency of the light pulse may be matched to the frequency of jetting in order to capture multiple images at the same point in the jet trajectory (with the apparent effect of a jet frozen in mid-flight) or with the frequencies slightly mismatched. When the frequencies are mismatched, each captured frame shows a jet at a slightly different point in its trajectory, giving the appearance of a jet slowly moving toward or away from the substrate.

Strobe imaging has been used to observe inkjet droplets in mid-flight [57]. The inkjet printing process is generally slower and therefore easier to capture than E-jet printing, but theoretically, strobe imaging should be able to capture E-jet printing as well as long as the process is repeatable and the pulse width of the strobe light is short enough to prevent motion blurring.

When using a strobe light to observe even fast events such as jetting, a standard video camera may be used. The exposure time is unimportant because the sensor is only illuminated during the event of interest, so motion blurring is not a concern. If a trigger is used to synchronize the start of the camera exposure with the strobe and jetting event, the event can be captured in one frame. Alternatively, the recording need not be synchronized with the camera. In this case, some frames will show the event and some will be dark.

The type of exposure the camera uses is important when using strobe imaging. While a CCD camera does not have a mechanical shutter, the manner in which the sensor is exposed is described using the terminology of “rolling shutter” or “global shutter”. A rolling shutter exposes different parts of the sensor at different times, while a global shutter exposes the entire sensor at once. Using a rolling shutter can cause problems called skew and wobble when trying to film moving objects because the image being detected changes position during the scan through the frame. Additionally, if a short, bright flash (in this case, a strobe light) occurs, it will cause part of the image to appear much brighter than the rest because the illumination is increased and/or decreased during the exposure of the image. This means that some pixels are captured in bright light while others are captured in dim light. There is no way to combat this problem other than to switch to a camera with a global shutter. An example of this problem is shown in Figure 3.5. Note in this image the dark bands at the top and bottom of the frame. In this case, the strobe pulse began after the exposure started and finished before the completion of the exposure.



Figure 3.5 Image captured using a standard CCD camera with a rolling shutter and a strobe light.

The strobe pulse width should be determined by the duration of the event to be observed. For this study, an LED with a strobe pulse width of $5\ \mu\text{s}$ was used in order to both provide enough light to give contrast to the image and reduce motion blurring.

Jetting does not occur immediately upon application of a high voltage to the nozzle. Some time is required for the Taylor cone to form and for the electrical force drawing the meniscus toward the substrate to overcome the surface tension force holding it close to the nozzle. Therefore, in order for the strobe flash to occur at the same time as the jet is produced, there must be a delay between the signals sent to the nozzle and to the strobe light. This delay timing should be on the order of microseconds and highly repeatable. A National Instruments sbRIO and FPGA were used to generate signals with high precision timing.

The camera used for the strobe imaging was a Vision Research Phantom 7 high speed camera. While a high speed camera is not required for strobe imaging, this camera was chosen because it has a global shutter and a sync function. By connecting the LED to the camera sync input, the start of the camera exposure was synchronized with the strobe flash and jetting. Figure 3.6 shows a schematic of the signals generated for strobe imaging.

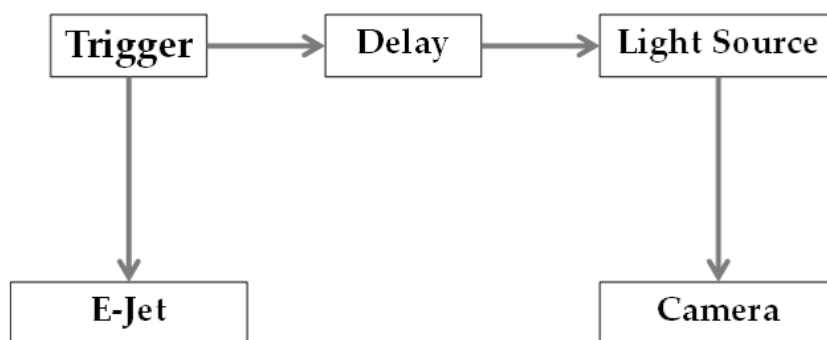


Figure 3.6 Schematic of signal generation for strobe imaging.

Capturing a jet in mid-flight was problematic because the jetting process has some variability in timing even under the same applied voltage, standoff height, ink type, and nozzle dimensions. When the same delay time was used in an attempt to capture multiple different jets at the same point in their trajectories, some jets were captured and others were not. Strobe imaging only works properly if there is a very high degree of repeatability in the event to be captured, so it was not effective in observing the jetting process.

3.3.2 High Speed Video

The second method used to observe the jetting process was to record high speed videos to capture each jet at multiple points in its trajectory. The drawback to using high speed video as compared to strobe imaging is that the number of data points per event is fundamentally limited by the frame rate of the camera. However, variability of the process does not inhibit data collection with this method.

High speed videos were captured using a Vision Research Phantom 7 camera. The frame rate was 66,666 frames per second so that frames are 15 μ s apart. An exposure time of 4 μ s was selected to balance the need for light intensity (longer exposure) and the need to eliminate blurring caused by very fast jet motion (shorter exposure). The resolution is 125 x 125 pixels.

Ideally, in order to develop a general model for E-jet ink ejection, inks with a wide range of properties should be studied. High-speed videos of three types of ink were taken for this study: a water/glycerol solution, a phosphate-buffered saline (PBS)/glycerol solution, and a UV-curable optical adhesive (NOA 74, Norland Products). However, only NOA 74 is included in the

analysis section. Both the water/glycerol and PBS/glycerol solutions produced jets which were too fast to capture enough frames to properly characterize the jet trajectory.

Figure 3.7 and Figure 3.8 illustrate the problem for water/glycerol solutions of two different concentrations. For both solutions, the entire jetting process occurs within four frames (60 μ s). With only four data points, it is difficult to characterize the jetting process. For these inks, a camera capable of recording video at a higher frame rate would be required to collect useful data. From a qualitative standpoint, however, a major difference between the glycerol solutions and NOA 74 is that the NOA 74 exhibits a cyclical pattern of multiple “drops” in rapid succession, while the glycerol solutions appear to produce only one drop at a time. Possible reasons for this difference will be discussed in more detail in the next chapter.

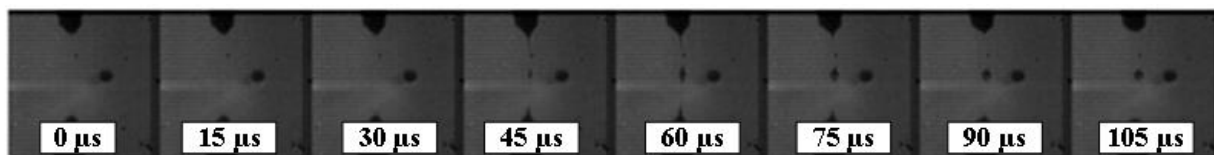


Figure 3.7 Frames from high-speed video of one jetting cycle of a 50% water/50% glycerol solution from a 10 μ m nozzle.

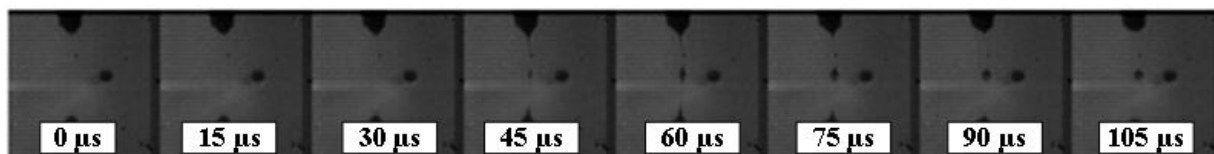


Figure 3.8 Frames from high-speed video of one jetting cycle of a 75% water/25% glycerol solution from a 10 μ m nozzle.

NOA 74 provided better results in the sense that it produced slower jets, which in turn allowed more data points to be collected. Using a 5 μ m nozzle, high-speed video of several full jetting cycles was recorded. Each of these cycles exhibited a distinct pattern of three drops, with the time elapsed between the second and third drops being slightly longer than the time elapsed between the first and second. Additionally, the jet only partially retracted toward the nozzle after the first drop. After the second drop, it retracted slightly farther. After the third drop, it returned to its original position at the beginning of the cycle. For each drop, when the jet reached the substrate, the tip of the jet broke off and remained on the substrate, while the tail retracted quickly.

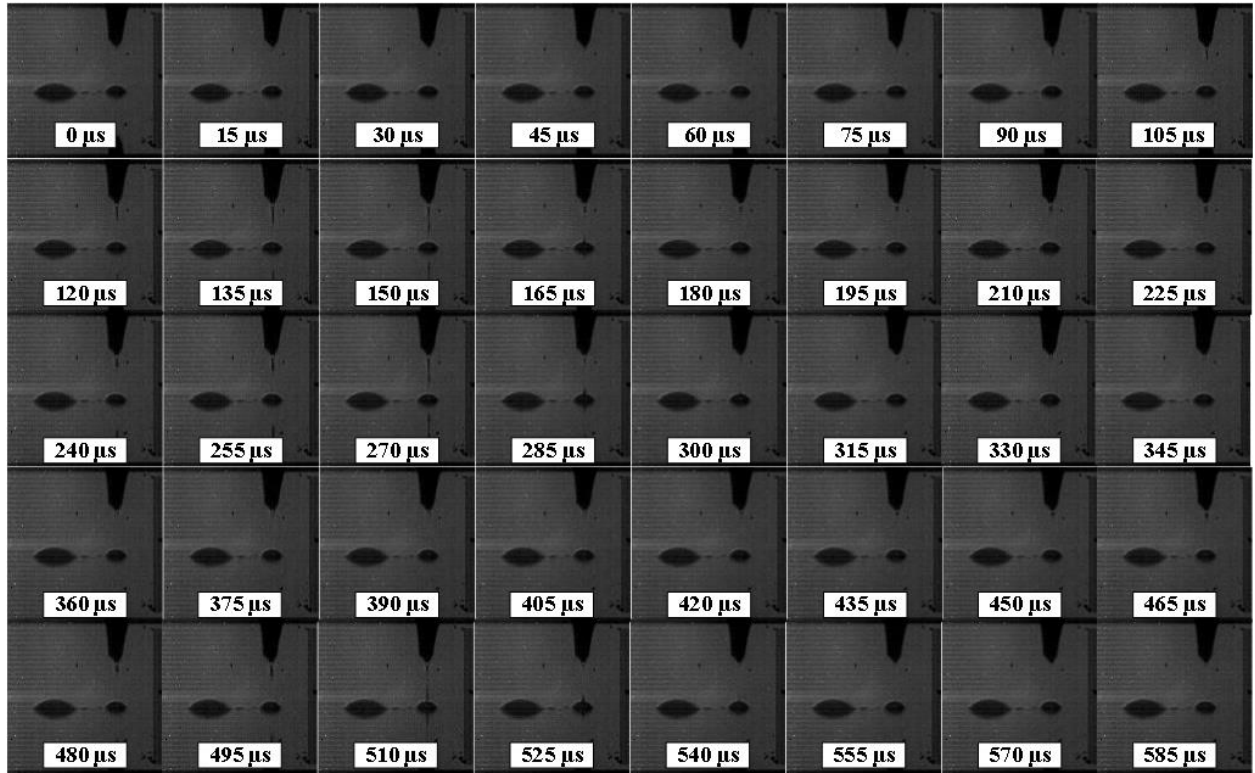


Figure 3.9 Frames from high-speed video of one jetting cycle of NOA74 from a 5 μm nozzle.

The results using a 10 μm nozzle were similar, but instead of the pattern of three drops, a pattern of four drops emerged. In the case of the first drop, instead of the typical immediate jet breakup and tail retraction upon reaching the substrate, the jet remained as a bridge between the nozzle and substrate for approximately 18 ms before retracting. During this time, ink flowed through the jet and continuously deposited on the substrate. The first drop phenomenon with the 10 μm nozzle seems to be a different type of ink deposition than is described by the mass-spring-damper model. The mass-spring-damper model does not attempt to describe a continuous flow type of behavior, but rather discrete deposition of small amounts of ink upon breakup of a jet. The second, third, and fourth drops with the 10 μm nozzle behaved like all three drops from the 5 μm nozzle. Frames from a full deposition cycle are not shown for the 10 μm nozzle because the length of the cycle is prohibitive.

3.3.3 Image Processing

The primary purpose for the video data collection was to observe the height of the jet tip as it moved from the nozzle to the substrate in the applied electric field. After capturing the jetting cycle in an .avi format, individual frames were extracted and saved using MATLAB. Figure 3.9 in the previous section shows an example of frames extracted for one jetting cycle.

For each frame, the height of the jet tip was determined using a standard process as follows. First, the image was cropped to the region of interest. The cropped image extends vertically from a few microns above the nozzle tip to the point where the droplet is left on the substrate. Since the reflection of the nozzle and jet was included in the original image, the entire reflection needed to be removed in order to identify the pixel(s) representing the tip of the actual jet. Figure 3.10 shows an example of a frame before and after cropping.

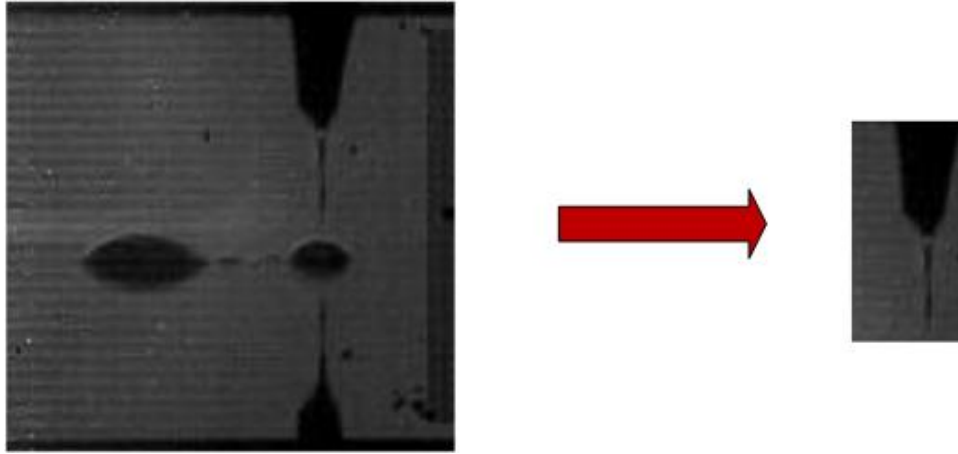


Figure 3.10 Frame from high-speed video before and after cropping to desired region.

The original video was captured in grayscale so that each pixel has an intensity value between 0 and 255. The next step was to select a threshold for the pixel intensity such that any pixel with a higher intensity (lighter colored) was converted to white, while any pixel with a lower intensity was converted to black. This step created a binary image with a clear distinction between the jet (black) and the background (white). Figure 3.11 shows the results of converting a grayscale image to a binary image.

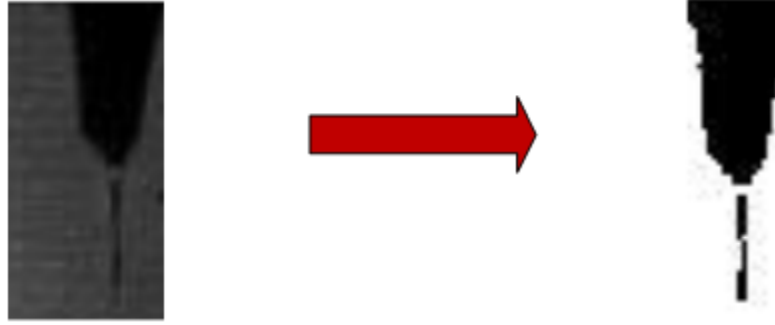


Figure 3.11 Conversion of grayscale image to binary image.

For model comparison purposes, only the tip of the jet is important. For each frame, a loop was run through the pixels to identify the black pixel with the largest row number, i.e., the lowest point included in the jet. In order to convert this pixel number to an actual height, the distance/pixel ratio was determined by counting the number of pixels across the bottom of the ink meniscus. Since the meniscus was anchored to the inner diameter of the nozzle, which was known to be either 5 μm or 10 μm , the scale of the image was determined by dividing the known length by the number of pixels. This scale factor was determined to be $\frac{5}{9}$ as illustrated in Figure 3.12.

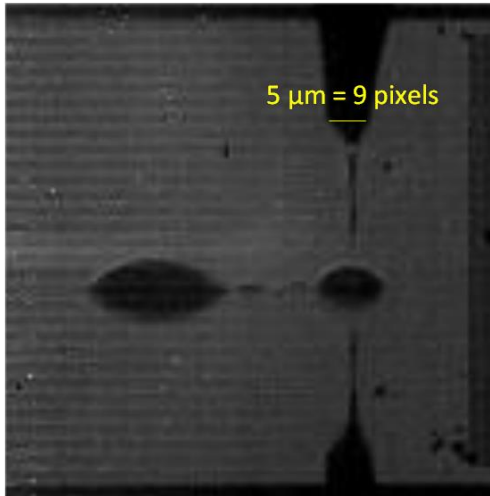


Figure 3.12 Distance/pixel scale factor determination.

Figure 3.13 shows that the initial reference point, $z_0 = 0$, for height z is defined as the stationary tip of the meniscus before jetting. The height of the substrate, z_s , is defined as the vertical distance from z_0 to the point at which the droplet hits the substrate. Note that z_s is a

positive value because z is defined as increasing in the downward direction. The height z of the jet tip was calculated using Eq. 3.5.

$$z = (\text{jet tip row \#} - \text{nozzle tip row \#}) * \text{scale factor} \quad (3.5)$$

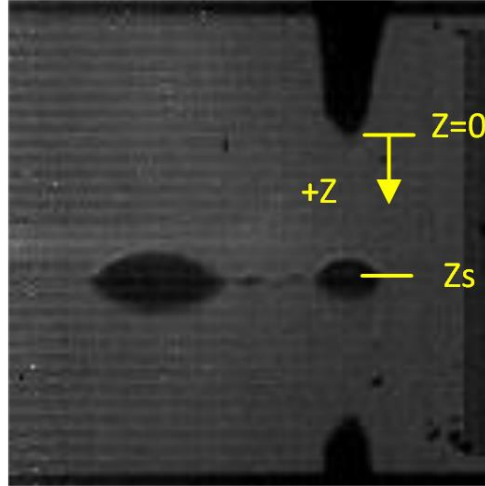


Figure 3.13 Definition of z_0 , z_s , and $+z$ direction.

After completing this image processing and data analysis for each frame in a video, with the knowledge that the time between frames in the video is $15 \mu\text{s}$, a plot of the height of the jet tip such as the one shown in Figure 3.14 is developed for the duration of the jetting cycle. The average height at each sample time across all seventeen test samples is shown in Figure 3.15. The error bars represent one standard deviation above and below the mean.

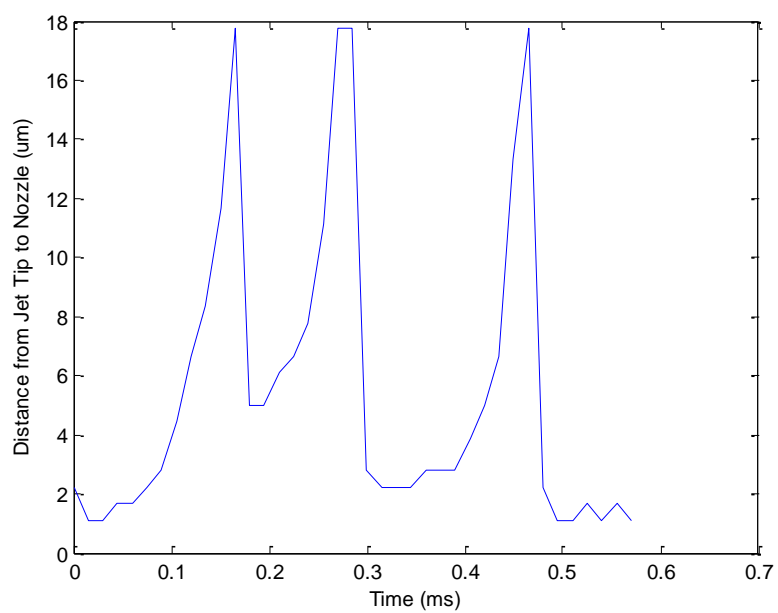


Figure 3.14 Height z of jet tip during one full jetting cycle of NOA 74 with a 5 micron nozzle.

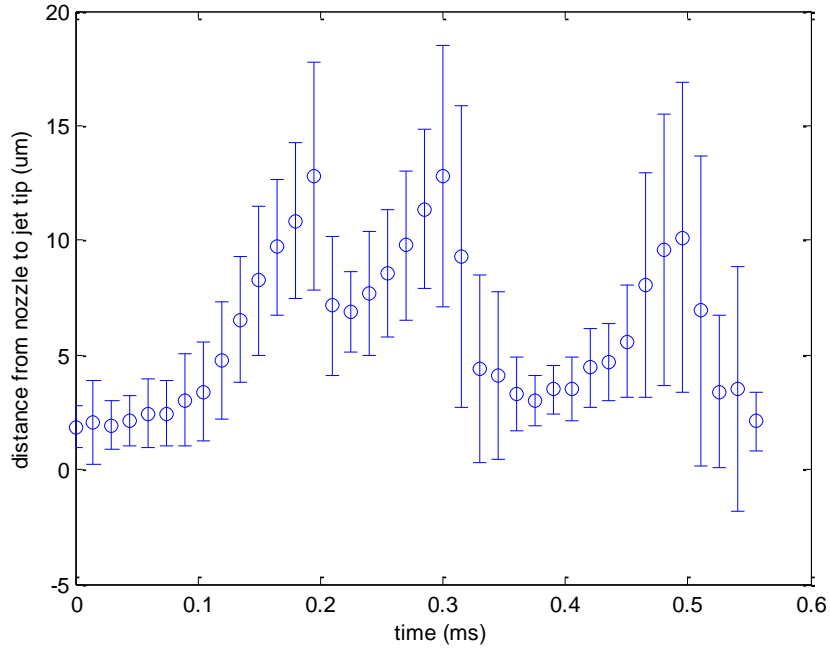


Figure 3.15 Average height z of jet tip at each sample time for all test samples of NOA 74 with a 5 micron nozzle. Error bars represent one standard deviation above and below the mean.

3.4 Model Parameter Determination

3.4.1 Conversion to Discrete Model

In order to find the best fit to the data obtained from the high-speed video analysis using the model developed previously, first a transfer function for the model is required. The input in the model is a forcing function based on the electric field, which is dependent on the position of the jet tip. Because the position of the jet tip is also the output of the system, the input of the system is dependent on its output.

We begin by defining a function U which depends on the position z of the jet tip in Eq. 3.6.

$$U = \frac{1}{(z_s - z)^2} \quad (3.6)$$

The transfer function for the system is then given by Eq. 3.7

$$\frac{Z(s)}{U(s)} = \frac{\frac{cq^2}{m}}{s^2 + \frac{b}{m}s + \frac{k}{m}} \quad (3.7)$$

In order to use the batch least squares method to find the best fit using the mass-spring-damper model, the continuous system model must be converted to a discrete model so that discrete data points can be used. The bilinear, or Tustin, transformation was implemented to find a discrete representation of the system. The Tustin transformation is based on approximating an integrator, $\frac{1}{s}$, using the trapezoidal rule. As a result, a substitution using Eq. 3.8 can be made with T as the sample period.

$$s = \frac{2(1-z^{-1})}{T(1+z^{-1})} \quad (3.8)$$

This substitution results in the discrete form of the transfer function given in Eq. 3.9. Note that this transfer function is of the general form given in Eq. 3.10. Where the coefficients are defined by Eq. 3.11 – 3.15.

$$\frac{Z(z)}{U(z)} = \frac{\left(\frac{cq^2/4m}{\frac{4}{T^2} + \frac{2b}{mT} + \frac{k}{m}}\right) + 2\left(\frac{cq^2/4m}{\frac{4}{T^2} + \frac{2b}{mT} + \frac{k}{m}}\right)z^{-1} + \left(\frac{cq^2/4m}{\frac{4}{T^2} + \frac{2b}{mT} + \frac{k}{m}}\right)z^{-2}}{1 + \left(\frac{-\frac{8}{T^2} + \frac{2k}{m}}{\frac{4}{T^2} + \frac{2b}{mT} + \frac{k}{m}}\right)z^{-1} + \left(\frac{\frac{4}{T^2} - \frac{2b}{mT} + \frac{k}{m}}{\frac{4}{T^2} + \frac{2b}{mT} + \frac{k}{m}}\right)z^{-2}} \quad (3.9)$$

$$\frac{Z(z)}{U(z)} = \frac{\beta_2 z^{-2} + \beta_1 z^{-1} + \beta_0}{-\alpha_2 z^{-2} - \alpha_1 z^{-1} + 1} \quad (3.10)$$

$$\beta_0 = \frac{cq^2/4m}{\frac{4}{T^2} + \frac{2b}{mT} + \frac{k}{m}} \quad (3.11)$$

$$\beta_1 = 2 * \frac{cq^2/4m}{\frac{4}{T^2} + \frac{2b}{mT} + \frac{k}{m}} \quad (3.12)$$

$$\beta_2 = \frac{cq^2/4m}{\frac{4}{T^2} + \frac{2b}{mT} + \frac{k}{m}} \quad (3.13)$$

$$-\alpha_1 = \frac{-\frac{8}{T^2} + \frac{2k}{m}}{\frac{4}{T^2} + \frac{2b}{mT} + \frac{k}{m}} \quad (3.14)$$

$$-\alpha_2 = \frac{\frac{4}{T^2} - \frac{2b}{mT} + \frac{k}{m}}{\frac{4}{T^2} + \frac{2b}{mT} + \frac{k}{m}} \quad (3.15)$$

The numerator contains three terms, but the coefficients β_1 and β_2 are multiples of β_0 . To represent this constraint, a new input variable, U^* , is defined in Eq. 3.16.

$$U^*(z) = (z^{-2} + 2z^{-1} + 1)U(z) \quad (3.16)$$

By this definition,

$$U^*(k) = U(k-2) + 2U(k-1) + U(k) \quad (3.17)$$

Then the discrete transfer function can be rewritten as shown in Eq. 3.18.

$$\frac{Z(z)}{U^*(z)} = \frac{\beta_0}{-\alpha_2 z^{-2} - \alpha_1 z^{-1} + 1} \quad (3.18)$$

3.4.2 Batch Least Squares Fitting

When parameters for a system with a given structure are to be determined based on a data set with more data points (and therefore more equations) than unknown parameters, the least squares method is a common way to find the best fit for the parameter values. Generally, the goal of the least squares method is to choose parameters which minimize the sum of the squared errors between the measured values and the values predicted by the parameters. When all of the data is collected and then fit to the model at once, the method is referred to as batch least squares fitting.

First a theta vector containing the coefficients to be determined must be defined. In this case, we would like to fit three coefficients (β_0 , α_1 , and α_2) to the data collected from the videos using the mass-spring-damper model. The theta vector containing the coefficients to be determined is defined in Eq. 3.19.

$$\theta = \begin{bmatrix} \alpha_1 \\ \alpha_2 \\ \beta_0 \end{bmatrix} \quad (3.19)$$

Next, a regression vector $x(k)$ composed of system inputs and outputs is defined. In this system, there are two outputs: $z(k-1)$ and $z(k-2)$. The only input is U^* as defined in Eq. 3.16.

$$x(k) = \begin{bmatrix} z(k-1) \\ z(k-2) \\ u^*(k) \end{bmatrix} \quad (3.20)$$

A vector Z represents the actual height of the jet tip in each frame. Note that the index begins at the third frame because each predicted height depends on the previous two time steps, and the length of the actual height vector should match the length of the predicted height vector.

$$Z = \begin{bmatrix} z(3) \\ z(4) \\ \vdots \\ z(M) \end{bmatrix} \quad (3.21)$$

Finally, a matrix Φ is composed of the regression vectors for each time step beginning at the third sample. The solution for the vector of coefficients $\hat{\theta}$ which minimizes the squared errors is determined using Eq. 3.23.

$$\Phi = \begin{bmatrix} x(3)^T \\ x(4)^T \\ \vdots \\ x(M)^T \end{bmatrix} \quad (3.22)$$

$$\hat{\theta} = (\Phi^T \Phi)^{-1} \Phi^T Z \quad (3.23)$$

Using this method, coefficients for the discrete system model were determined for each of the three drops in five jetting cycles. These values, along with their averages and standard deviations, are listed in Table 3.1. The standard deviations for the coefficients are large compared to the average values, which may be an indication that the coefficients have not been correctly identified or that the process varies between cycles.

Table 3.1 Coefficients for discrete model determined using batch least squares method.

Test #	Drop 1			Drop 2			Drop 3		
	β_0	α_1	α_2	β_0	α_1	α_2	β_0	α_1	α_2
1	-2.929	-1.214	-0.016	20.111	-2.052	1.101	162.948	0.179	-0.653
2	9.120	-0.645	-0.654	23.694	-1.526	0.601	199.888	-1.045	0.960
3	19.749	-0.932	-0.090	84.489	-0.818	0.157	125.828	-1.526	1.084
4	--	--	--	1.135	-1.091	-0.067	43.403	-0.342	-0.670
5	5.123	-1.111	-0.074	25.968	-1.244	0.276	4.326	-0.430	-0.812
Average	7.766	-0.975	-0.209	31.079	-1.346	0.414	107.278	-0.633	-0.018
Std. Dev.	9.431	0.249	0.299	31.425	0.470	0.454	81.699	0.662	0.953

3.4.3 Parameter Ratio Solutions

The three discrete model coefficients collectively describe four system parameters: mass, charge, damping coefficient, and spring constant. The three discrete model coefficients cannot determine all four system parameters. However, the system of equations can be solved for three ratios of parameters: $\frac{cq^2}{m}$, $\frac{b}{m}$, and $\frac{k}{m}$. The model describing the position of the jet tip can incorporate these ratios rather than the actual parameters. For the discrete model coefficients above, Table 3.2 shows the corresponding parameter ratios.

Table 3.2 Parameter ratios for mass-spring-damper model calculated from discrete coefficients.

Test #	Drop 1			Drop 2			Drop 3		
	cq^2/m	b/m	k/m	cq^2/m	b/m	k/m	cq^2/m	b/m	k/m
1	-3.8E+11	1.2E+05	-1.9E+09	1.4E+12	-6.5E+03	2.1E+08	2.8E+14	2.6E+06	5.6E+10
2	2.6E+12	4.5E+05	-5.4E+09	2.2E+12	3.4E+04	4.3E+08	1.9E+13	3.5E+03	5.4E+09
3	2.8E+12	1.2E+05	1.4E+09	1.2E+13	1.1E+05	3.1E+09	9.9E+12	-6.2E+03	2.7E+09
4				1.6E+11	1.4E+05	-1.4E+09	1.8E+13	6.6E+05	-3.2E+08
5	7.2E+11	1.4E+05	-1.6E+09	2.9E+12	7.7E+04	2.3E+08	2.0E+12	7.8E+05	-7.0E+09
Average	1.4E+12	2.1E+05	-1.9E+09	3.7E+12	7.1E+04	5.1E+08	6.6E+13	8.1E+05	1.1E+10
Std. Dev.	1.5E+12	1.6E+05	2.8E+09	4.7E+12	5.9E+04	1.6E+09	1.2E+14	1.1E+06	2.5E+10

The large variation in parameter ratios can be attributed to a lack of persistent excitation of the system, which is a requirement to guarantee correct parameter identification. In this case, persistent excitation would require oscillation in position of the jet, which would in turn necessitate very fast and precise control over voltage applied to the nozzle as well as very fast imaging.

Because persistent excitation cannot be achieved, there is no guarantee that the coefficients determined using the batch least squares method are correctly identified. However, as will be shown in the following sections, they can be used as a starting point to find parameters which cause simulation output to closely match the data.

3.4.4 Single Drop Simulation

In the first attempt to simulate a single drop, the average parameter ratios from Table 3.2 for the second drop were incorporated into the model. The first drop parameter averages were not

chosen for the simulation because the average $\frac{k}{m}$ value was negative. A negative value would indicate that the tail was pushing the droplet away instead of pulling it back toward the nozzle, which does not match the physical system. It should be noted that the standard deviation for $\frac{k}{m}$ is larger than the average value. With such a wide variation in the data, and considering the lack of persistent excitation mentioned previously, it is not surprising that the average value violates our physical intuition about the system.

With the parameter ratio values for the second drop, Figure 3.16 shows the height of the jet tip over time. The trajectory differs from the drop trajectories observed in two major ways. First, the shape of the curve is almost linear in the beginning for the simulated trajectory. Second, the jet takes just over 0.21 ms to go from its starting position near the nozzle to the substrate in simulation, while the actual jet takes only about 0.18 ms to reach the substrate.

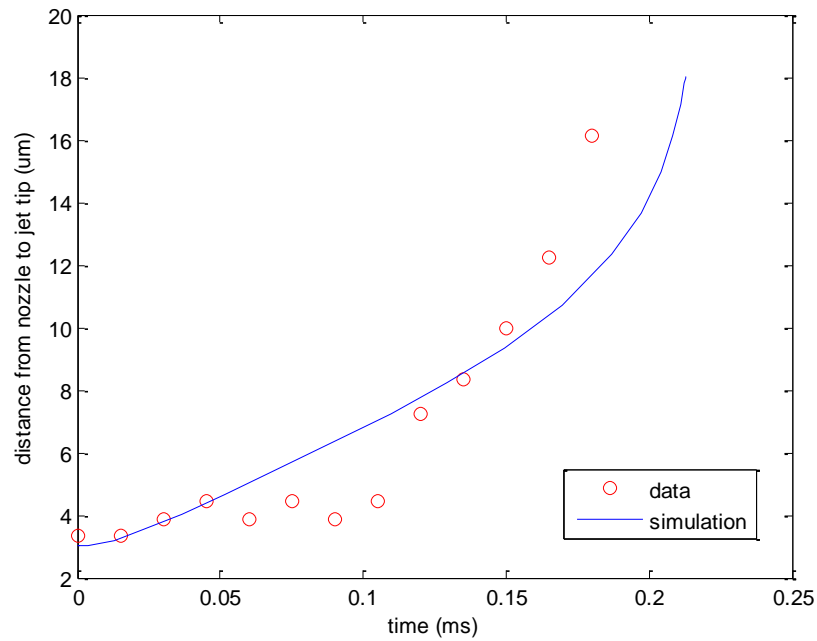


Figure 3.16 Height z of jet tip during a single drop simulation using average calculated parameter ratios.

While using the calculated parameters in the mass-spring-damper simulation gives a result which is qualitatively fairly similar to the actual data, some parameter tuning is required to improve the shape of the trajectory and time elapsed during a drop.

3.4.5 Parameter Tuning

The slope of the height vs. time graph is too straight at the beginning because the stiffness and damping terms contribute too heavily to the force balance. When the stiffness and damping constants are reduced, the jet tip has a greater acceleration early in its flight. The shape of the curve more closely approximates the actual height measurements. After adjusting the stiffness and damping, the value for $\frac{cq^2}{m}$ was chosen to make the time elapsed during the drop match the data. The tuned parameters are listed in Table 3.3.

Table 3.3 Tuned parameter ratios for mass-spring-damper model.

$\frac{cq^2}{m}$	$\frac{b}{m}$	$\frac{k}{m}$
1×10^{12}	7×10^3	5×10^7

Figure 3.17 shows the data for the first drop of Test 5 along with the simulation results using both calculated and tuned parameters.

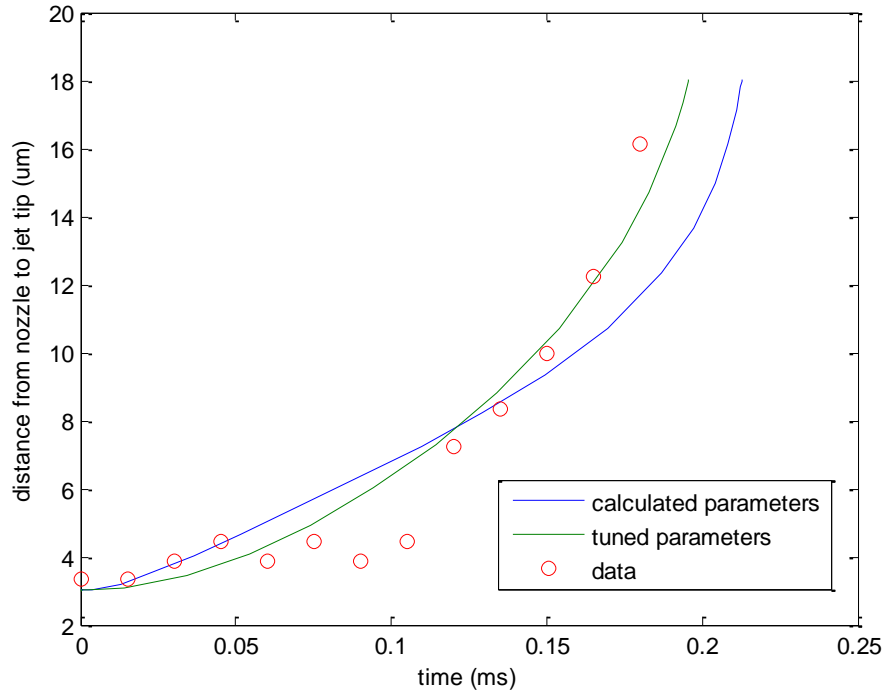


Figure 3.17 Height z of jet tip during a single drop from data and simulations using calculated or tuned parameters.

The tuned parameters cause the model output to match the data slightly more closely than do the calculated parameters in terms of both shape and timing, but the tuned parameters are within an order of magnitude of the calculated values.

3.4.6 Comparison of Mass-Spring Model to Physical Property-Based Approach

So far, we have used a set of system parameters which cause the simulation output to closely match the data gathered for jetting. We selected this set of parameters based on the mass-spring-damper system analogy. The parameters for mass and charge should correlate to the same physical values in the system. However, the stiffness value k and the damping constant b do not precisely correlate to physical properties.

As a check on the validity of this simplified second-order model using non-physical b and k parameters, we will compare it to a slightly more complex version based on physical forces. Keeping the assumptions of a point mass and charge in the jet tip, and calculating the

force exerted on the jet due to the electric field in the same way, consider the forces acting on the jet tip. In addition to the electrical force, a gravitational force also pulls the jet downward. Both a drag force due to air resistance and a damping force due to extensional viscosity of the ink exert a force in the direction opposite to the motion of the jet. A surface tension force holds the jet to the nozzle. The resulting force balance is given by Eq. 3.24 .

$$m\ddot{z} = F_\gamma + F_{\eta_e} + F_g + F_d + F_e \quad (3.24)$$

In the above equation, F_e is calculated in the same way as in our simplified model. F_g is simply the gravitational force, mg .

The definition of surface tension is the work required to increase the area of a liquid divided by a unit area. In this case, assuming that the tail of the jet is approximately cylindrical, the work required to move the jet toward the substrate by an amount dz is given by Eq. 3.25.

$$dW = F_\gamma dz = \gamma dA = 2\pi r_{tail} \gamma dz \quad (3.25)$$

Where γ is the surface tension of the ink and r_{tail} is the radius of the jet tail. Eliminating dz from both sides of the equation, and assuming that the radius of the jet tail is approximately constant during the drop, the force due to surface tension is a constant value given by Eq. 3.26.

$$F_\gamma = 2\pi r_{tail} \gamma \quad (3.26)$$

For a Newtonian fluid, the extensional viscosity is three times the shear viscosity. It is defined by the normal stress divided by the rate of strain as shown by Eq. 3.27.

$$\eta_e = \frac{\sigma_n}{\dot{\epsilon}} = \frac{F/A}{(1/z)(dz/dt)} \quad (3.27)$$

This allows us to calculate the force due to the extensional viscosity as shown in Eq. 3.28 . Note that this force is nonlinear.

$$F_{\eta_e} = \frac{\pi r_{tail}^2 \eta_e \dot{z}}{z} \quad (3.28)$$

In order to calculate the drag force on the jet, we need to calculate the Reynolds number in order to know which equation for drag is appropriate. The Reynolds number is calculated using Eq. 3.29.

$$Re = \frac{\rho_d v L}{\mu} \quad (3.29)$$

Where ρ_d and μ are the density and viscosity of air at room temperature, v is the velocity of the jet, and L is the characteristic length of the jet, in this case its diameter. We can approximate v in this calculation by taking the distance from the nozzle to the substrate and dividing by the time elapsed during a drop, which gives a value of approximately 8.3×10^{-2} m/s. The value for Re is then approximately 0.005 for a jet with a diameter of 1 μm . Because this value is less than one, we can approximate the drag force on the jet using Stokes' formula given in Eq. 3.30).

$$F_d = -6\pi\mu_{air}r_{tail}\dot{z} \quad (3.30)$$

A simulation of this model gives the height shown in Figure 3.18. The mass of the jet tip was estimated based on the density of the ink and the size of the droplet. The charge on the jet tip is not known, but was selected to bring the time elapsed during a drop reasonably close to the observed jetting time.

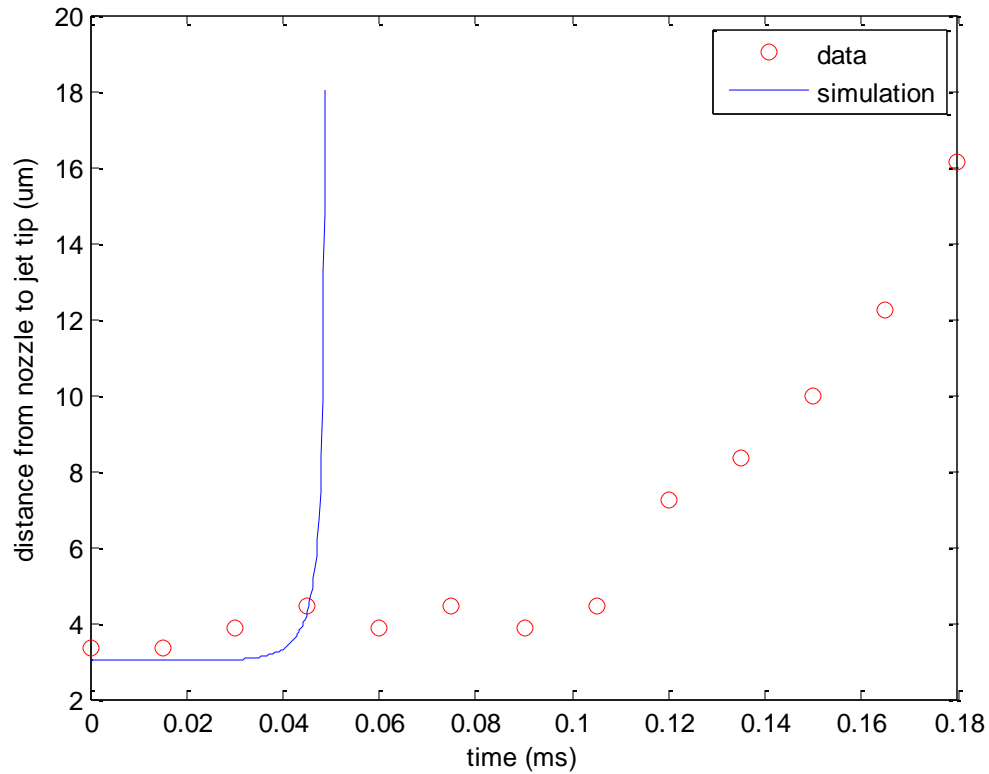


Figure 3.18 Height z of jet tip during a single drop from data and simulation using physical property-based modeling.

This model is actually a worse fit to the observed trajectory of the jet tip, which could mean that the point mass and charge assumptions are poor, the parameter values used in the model are incorrect, or that there are other forces which need to be considered. While a model based purely on physical principles has the potential to be more accurate than the mass-spring-damper model presented in this chapter, it would require much more extensive study, which comes at a cost. This section demonstrates that a white-box model can provide very poor results using reasonable estimates for the parameters. For researchers who do not wish to invest the time and effort into developing a highly accurate white-box model, our gray-box model can serve as a tool which gives accurate results while needing to match fewer parameters.

3.5 Summary

In this chapter, we have presented a gray-box second-order system model as a representation of a single drop of a jet cycle during E-jet printing. Compared to a white-box model which attempts to fully describe the system based on first principles, our approach generates a model which will be more useful for applications which require a lower degree of computational complexity. Even though the model is not directly derived from first principles, its output closely matches the height of the jet as observed with a high-speed camera. In the next chapter, we will expand this model to describe a jet cycle, during which multiple drops may occur as shown in Figure 3.14 above.

Chapter 4

Jet Cycle Modeling and Validation

4.1 Introduction

In the last chapter, a gray-box second-order model was used to describe the height of the jet tip during a single drop. In this chapter, we expand our modeling approach to consider the full jetting cycle, including multiple drops and retractions of the jet.

For the 5 μm nozzle, 40 jetting cycles were captured. In each cycle, there were three “drops”, that is, the jet extended to the substrate and subsequently retracted three times. The first retraction did not return the jet tip all the way to its initial position, and the second drop occurred in quick succession after the first. The second retraction brought the jet tip closer to its initial position, and a longer time period elapsed from the second to third drop as compared to the first to second drop. The third retraction brought the jet tip back to its initial position.

In this chapter, we will present two approaches to full-cycle jet modeling. In the first, jetting is split into three separate modes: drop, retraction, and build. The second method contains only one mode in which the parameters are constantly changing. In both methods, the mass-spring-damper system is a hybrid system. The parameter ratios used in the model undergo both continuous changes in some or all modes as well as discrete changes between modes.

Both modeling methods were developed to match the representative data set from Test 5 shown in the previous chapter. To evaluate the validity of the models for general jetting cycles under the same test conditions, the average and standard deviation of the jet tip height across all tests are presented and compared to the simulation results.

4.2 Three-Mode Switched-System Model

In this section, we will use the same model structure with constant parameters that we used in Chapter 3 as the drop mode, and also add retraction and build modes. These three modes together will be used to describe the production of multiple droplets during one complete jetting cycle. Figure 4.1 shows the order of events in a general cycle.

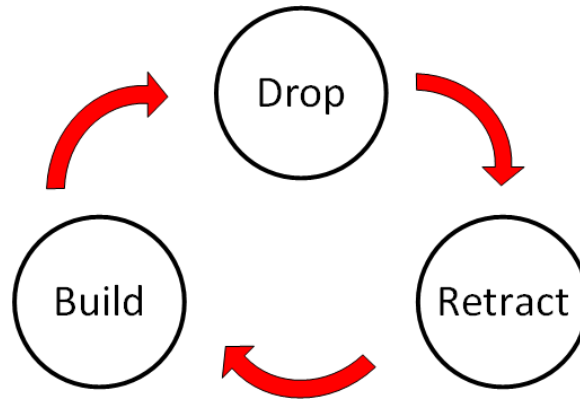


Figure 4.1 Diagram of three-mode jet cycle.

For the particular ink and E-jet system properties used in our experiments, there were three drop modes, three retraction modes, and two build modes. Figure 4.2 highlights the modes on the data set from Test 5 which was shown in the previous chapter.

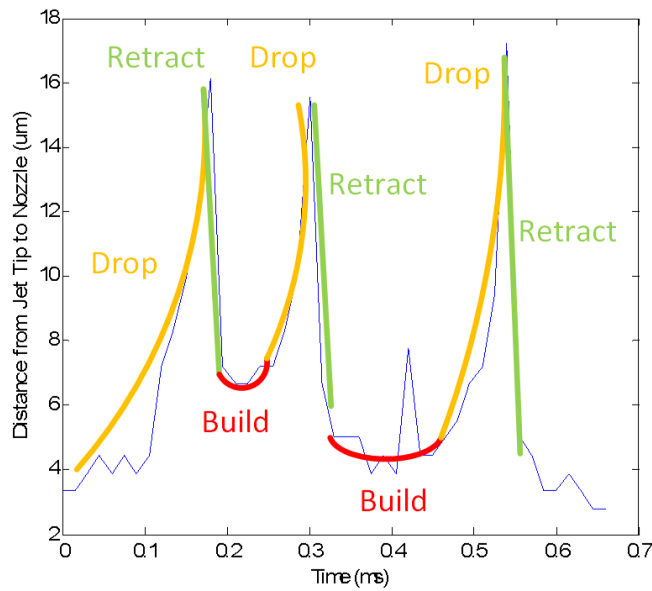


Figure 4.2 Illustration of drop, retraction, and build modes with height data from Test 5.

4.2.1 Jet Retraction

In order to understand the reason for jet retraction, recall that the jet is driven toward the substrate by an electric field acting on the charged tip. When the jet reaches the substrate, the tail begins to thin and create a neck before completely separating, leaving most of the tip of the jet on the surface of the substrate. This causes both the mass and charge on the jet tip to decrease instantaneously. Due to the decrease in charge, the electrical force on the jet tip also decreases. The spring-to-mass and damping-to-mass parameter ratios increase due to the loss of mass. The balance of forces is reversed due to the loss of charge so that the spring force is stronger than the electrical force, and the jet is pulled back toward the substrate.

The parameters for the retraction mode were selected to match the data set from the test shown in the previous chapter. As explained above, the parameter ratios $\frac{b}{m}$ and $\frac{k}{m}$ increase instantaneously upon entering the retraction mode due to a loss in mass with the assumption that b and k remain the same. This assumption is based on the idea that b and k are related to physical properties of the ink (e.g., surface tension) contained in the tail of the jet, which do not change when the tip of the jet breaks away. The values for the parameters during the retraction mode are the same for each drop in the cycle, and they are listed in Table 4.1.

Table 4.1 Parameter ratios during retraction mode for all drops in jetting cycle.

$\frac{cq^2}{m}$	$\frac{b}{m}$	$\frac{k}{m}$
1×10^9	6.8×10^5	7.5×10^{10}

In our experiments, the jet tip does not break off until it hits the substrate. This is not necessarily true for all inks under all conditions. However, for this model, we can define the switching criterion from drop mode to retraction mode as the tip of the jet reaching the substrate. This is equivalent to the condition that $z = z_s$.

4.2.2 Build Mode

A third mode is needed in order to address the elapsed time between a jet retraction and subsequent drop. From the height plot for the full cycle, the jet appears to remain at

approximately the same height for a short time after retraction. This time period is slightly longer between the second and third drops than between the first and second drops.

This third mode, which we call the *build* mode, provides a gradual parameter transition between the jet retraction and drop modes. While a discrete change in parameters makes sense when the jet tip breaks off (charge and mass are immediately lost), there is no sudden change in the physical system between the time when the jet stops its retraction and when it begins to drop again. Instead, mass and charge should increase continuously as the tip of the jet grows until the electrical force drawing the jet toward the substrate once again exceeds the spring force drawing it toward the nozzle. Unlike the drop and retraction modes, therefore, the parameter ratios should change during the build mode. We will assume that this change is linear.

The condition for switching from the retraction mode to the build mode is that the jet tip becomes close enough to the nozzle. This condition is chosen based on the value of z when it “levels out” from the Test 5 data set. For the first switch from retraction to build mode, this value is approximately 6 μm , and for the second switch, it is approximately 4 μm . However, these values cannot be used as the switching conditions because the height does not immediately level out. The switching condition must be set to a z value greater than the desired height to account for this lag. In this case, the first switching condition was set to $z = 7$, and the second was set to $z = 5$.

Ideally, the initial value for each parameter ratio should be its value during the retraction mode. Practically speaking, however, this gives poor results as shown below. Additionally, the rates of change for the parameter ratios should theoretically be chosen so that the parameter ratios upon exiting the build mode are equal to their values in the subsequent drop mode. This would cause the parameter ratios to be continuous during the build-to-drop mode switch. Again, with these rates, the height of the jet tip in the simulation does not match the data. Figure 4.3 shows the results of a simulation using the retraction mode parameter ratio values as the initial conditions and derivatives chosen so that the final values of the parameter ratios during the build mode match those of the subsequent drop mode. Figure 4.4 shows the parameter ratio values during the same simulation. These results do not make physical sense because in order for z to be less than zero, the jet tip would have to reenter the nozzle, which we did not observe.

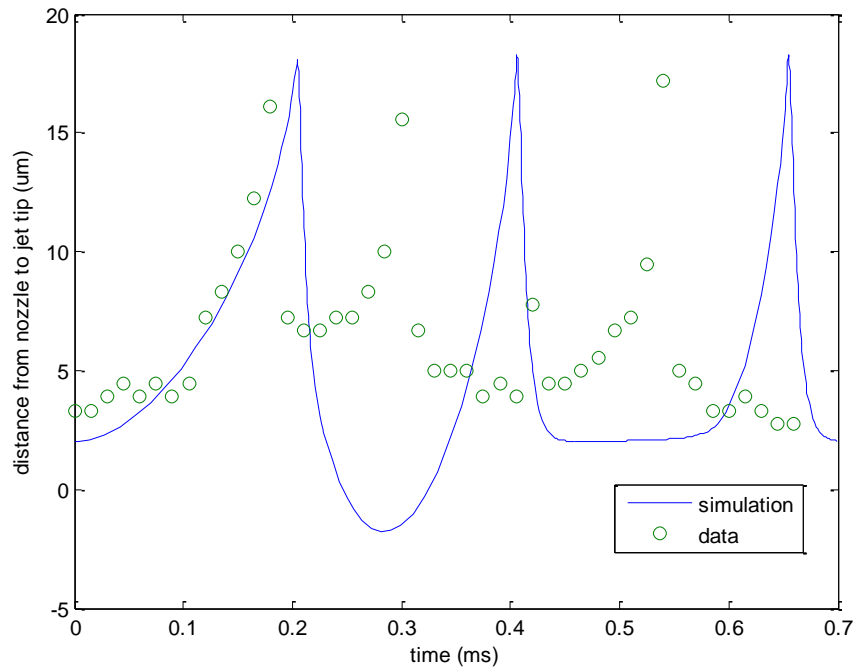


Figure 4.3 Height z of jet tip during a full jetting cycle from data and simulation using three-mode parameter model with build rates chosen to keep parameter ratios continuous across modes.

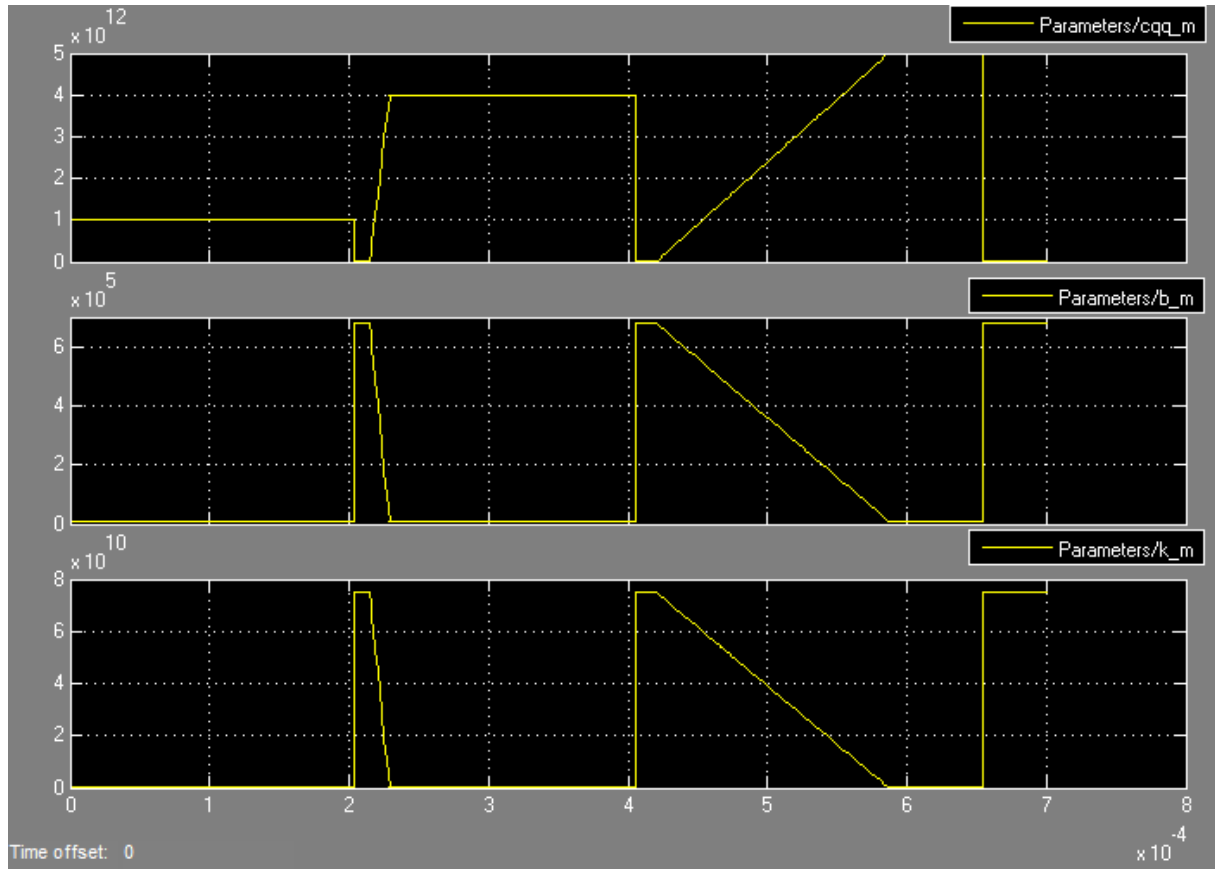


Figure 4.4 Parameter ratios during full jetting cycle simulation using drop, retraction, and build modes. Parameter ratios are continuous from retraction to build mode and from build mode to drop mode.

Instead, we use the rates given in Table 4.2 for the parameter ratio changes along with a discrete change in the $\frac{k}{m}$ value from 7.5×10^{10} to 7.5×10^9 at the beginning of the build mode. While this causes the model to match the data better, it no longer fits our intuition behind the build mode, which is to maintain continuity between parameter ratio values from retraction to build and build to drop modes. Figure 4.5 illustrates these discontinuities in parameter ratios.

Table 4.2 Rates of change of parameter ratios during first and second build modes.

	$\frac{d}{dt} \left(\frac{cq^2}{m} \right)$	$\frac{d}{dt} \left(\frac{b}{m} \right)$	$\frac{d}{dt} \left(\frac{k}{m} \right)$
First Build Mode	3×10^{17}	-1×10^9	-1×10^{14}
Second Build Mode	3×10^{16}	-1×10^9	-5×10^{13}

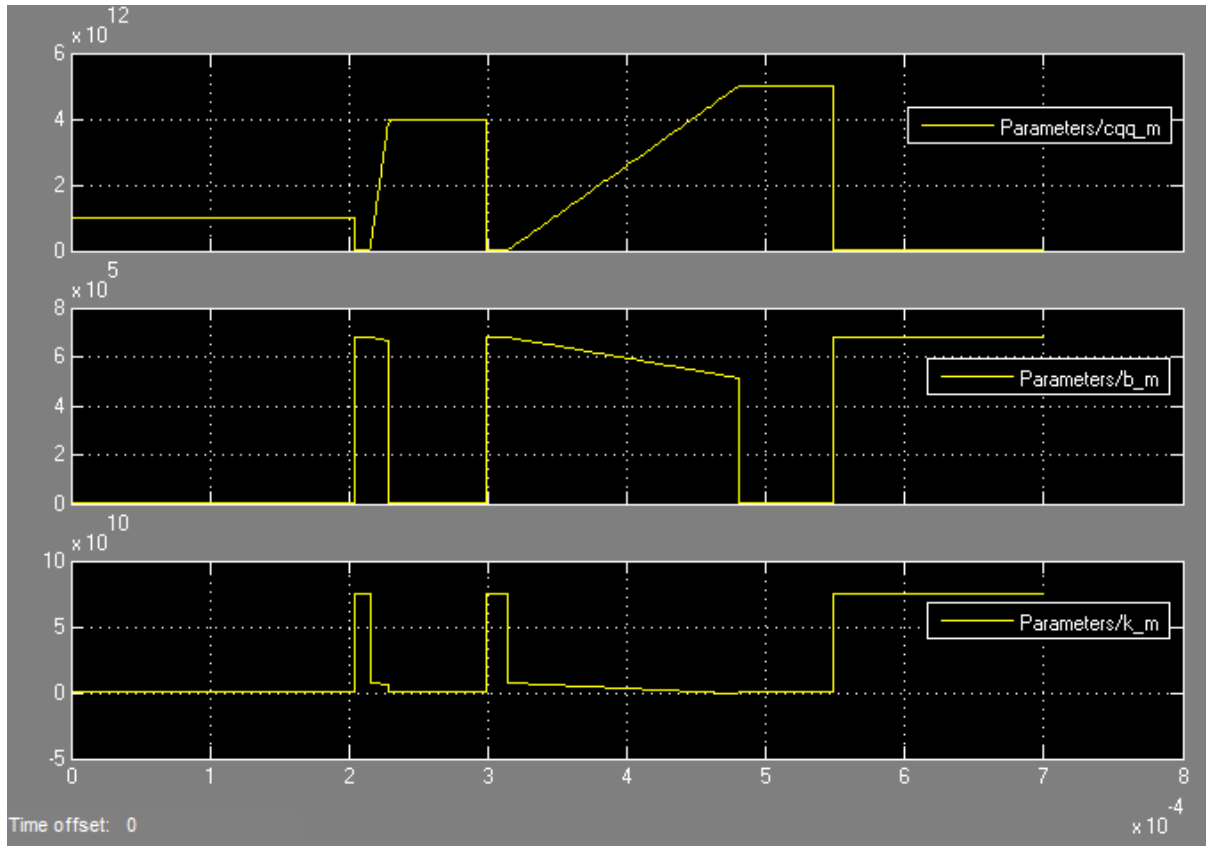


Figure 4.5 Parameter ratios during full jetting cycle simulation using drop, retraction, and build modes. Parameter ratios have discontinuities between modes.

4.2.3 Parameter Ratio and Drop Number Relationship

Each parameter ratio is constant within a drop mode, but the value of $\frac{cq^2}{m}$ depends on the drop number—i.e., whether the drop is first, second, or third in the cycle. In the previous chapter, the parameter ratio values were tuned to match the first drop, so the same values were used in the first drop of the full cycle. The parameter ratio values for each drop are listed in Table 4.3. Note that $\frac{cq^2}{m}$ increases with each drop. This matches the trend from the five data sets to which we fit parameters in the previous chapter. A possible explanation for this observation is that the charge on the jet tip builds up more quickly than mass is added to the jet tip. The rapid increase in charge causes the jet to drop again before the mass builds up to the same amount as in the

previous drop. Unlike $\frac{cq^2}{m}$, $\frac{b}{m}$ and $\frac{k}{m}$ are the same during each drop mode. From the parameter fitting for the five data sets in the previous chapter, there is no clear trend for these parameter ratios from drop to drop.

Table 4.3 Parameter ratio values during first, second, and third drop modes of a jetting cycle.

	$\frac{cq^2}{m}$	$\frac{b}{m}$	$\frac{k}{m}$
First Drop Mode	1×10^{12}	7×10^3	5×10^7
Second Drop Mode	4×10^{12}	7×10^3	5×10^7
Third Drop Mode	5×10^{12}	7×10^3	5×10^7

4.2.4 Stateflow Implementation

In the previous chapter, the height of a single drop was modeled using Simulink. For the full jetting cycle, we must modify our previous Simulink model to reflect the additional modes we are now considering. A Stateflow block was added to determine the parameter ratio values to be used in the Simulink model based on the current system mode. Stateflow is a software environment which facilitates modeling and control of hybrid and switched systems. It allows the user to define modes and the switching criteria between those modes, and state variables and parameters may exhibit both continuous and discrete behavior. The modes and switching criteria for the three-mode switched-system model were described in previous sections. Figure 4.6 is a Stateflow diagram showing the implementation of this parameter ratio switching logic.

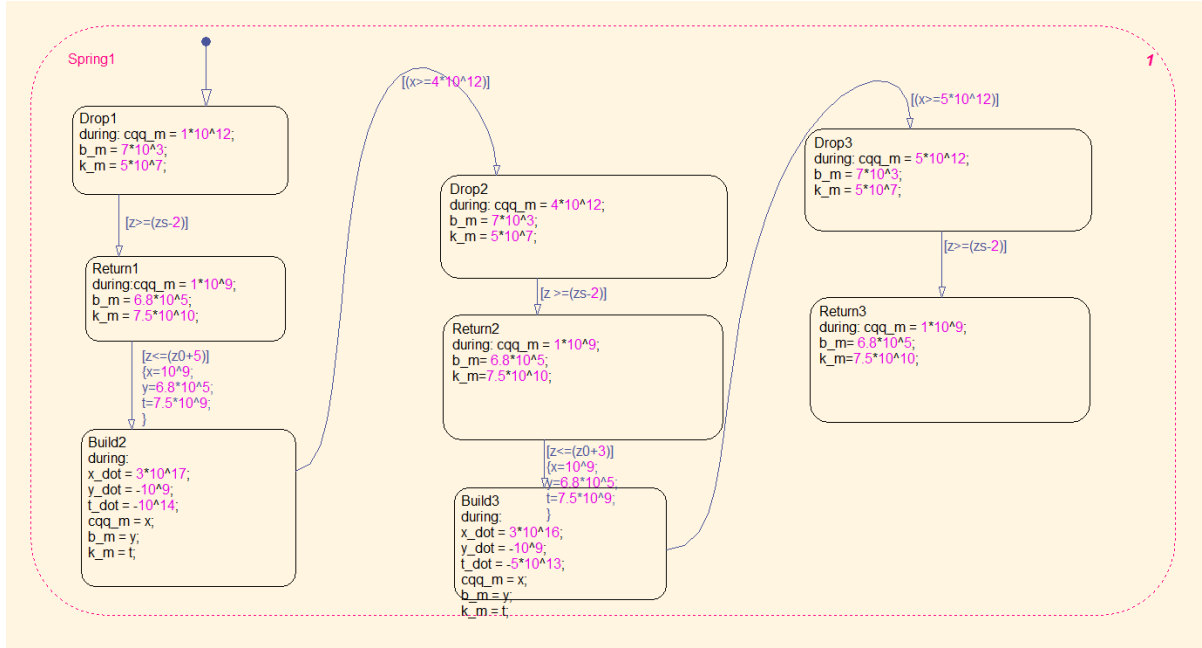


Figure 4.6 Stateflow diagram for determination of parameter ratio values during full jetting cycle with multiple drop, retraction, and build modes.

4.2.5 Results and Analysis

Figure 4.7 shows the results of the simulation of a full jetting cycle using the three-mode switched-system model described in this section with the data from the full Test 5 jetting cycle overlaid. For this drop-retraction-build approach to parameter determination, the simulation results fit the data well. The peaks in the simulation occur at approximately the correct times, and the jet retracts between drops to approximately the correct height as expected because the parameters were chosen to fit this data set.

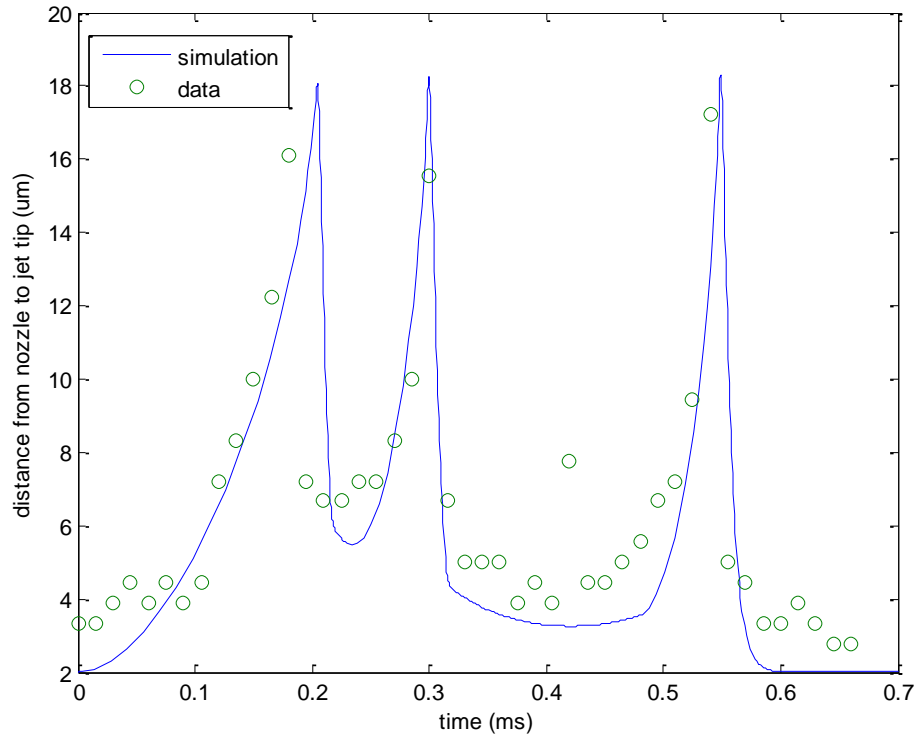


Figure 4.7 Height z of jet tip during a full jetting cycle from data and simulation using three-mode parameter model.

The validity of this model to describe other test sets using the same ink and setup is evaluated in Figure 4.8. This plot shows the average height at each time over all seventeen data sets with error bars representing one standard deviation above and below the average values. The simulated height lies within one standard deviation from the mean for the first two drops of the cycle. The simulated third drop occurs about 50 μs later than the third drop in the average of the data sets. This is a consequence of the slight variation in drop times between tests. Overall, the drop-retraction-build method gives a close match to the data for all cycles.

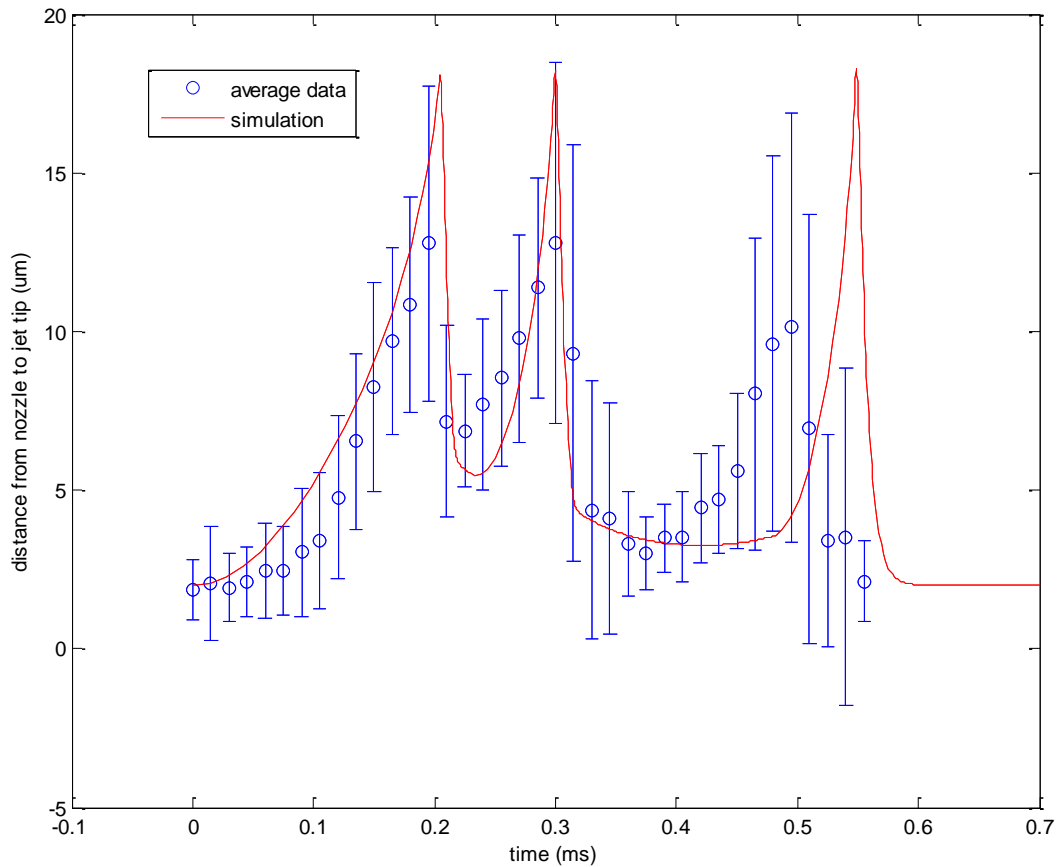


Figure 4.8 Comparison of height of jet tip during a full jetting cycle from simulation using three-mode parameter model and mean height during all data sets with error bars representing one standard deviation above and below the mean.

However, there are some drawbacks to this method. The goal of the build mode was to bridge the gap between retraction and drop modes and force continuity in the parameter ratios during the transition, but in order to match the data, some discrete changes in parameter ratios still needed to be included for which there is no clear physical basis. Additionally, the switching conditions were chosen arbitrarily based on the jet tip height to match the leveling off seen during the build mode, but this does not provide an explanation for why the mode switch occurs at that point or why the jet switches from retracting to dropping. The three-mode switched parameter ratio model, while accurately descriptive of the jetting events observed in our

experiments, does not give a complete explanation for certain aspects of the cycle. The single-mode cycle discussed in the following section attempts to address these concerns.

4.3 Single-Mode Switched-System Model

In the previous section, two of the drawbacks mentioned for the drop-retraction-build method were that the switching criteria between modes were based solely on matching to the data, providing no intuitive explanation for when or why the change should occur, and that there were some discrete parameter changes required to fit the data which have no physical basis. In this section, we will eliminate both of these issues by considering a single mode which encompasses the entire evolution of a drop.

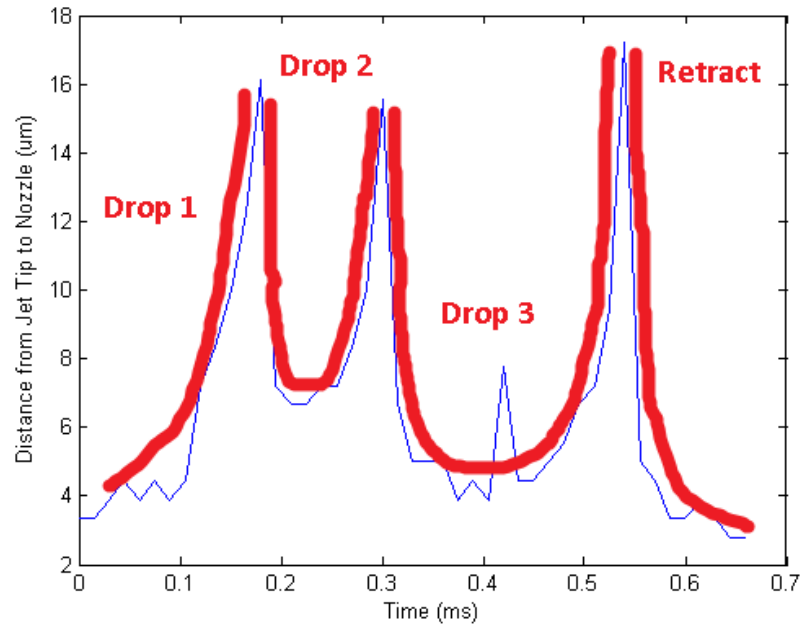


Figure 4.9 Illustration of single (drop) mode occurring multiple times during a jetting cycle.

4.3.1 Modeling and Stateflow Implementation

Recall that in our previous method, we used the build mode as a bridge between the parameters of the retraction mode and those of the drop mode. We will now expand on this idea.

Rather than assuming that parameters remain constant while a jet drops and retracts, we treat the mass and charge as continuously increasing quantities. However, now we will treat the change as a first-order response instead of a linear change. The parameter ratios $\frac{b}{m}$ and $\frac{k}{m}$ decrease during a drop mode as the mass increases and approach a lower limit. The ratio $\frac{cq^2}{m}$ increases as both charge and mass increase and approaches an upper limit. The limits should correspond roughly to the constant parameters of the drop mode in our previous drop-retraction-build model. For the parameters to have a first-order response, their derivatives should be of the form given in Eq. 4.1, where x is the parameter ratio, x_f is the limit that the parameter ratio approaches, and τ is the time constant of the response. Table 4.4 lists the derivatives of the parameter ratios during the three drops.

$$\dot{x} = \frac{1}{\tau}(x_f - x) \quad (4.1)$$

Table 4.4 Derivatives of parameter ratios during first, second, and third drop modes of a jetting cycle.

	$\frac{d}{dt}\left(\frac{cq^2}{m}\right)$	$\frac{d}{dt}\left(\frac{b}{m}\right)$	$\frac{d}{dt}\left(\frac{k}{m}\right)$
Drop 1	$10^5 \left(1.2 \times 10^{12} - \frac{cq^2}{m}\right)$	$10^5 \left(7 \times 10^3 - \frac{b}{m}\right)$	$10^5 \left(5 \times 10^7 - \frac{k}{m}\right)$
Drop 2	$2 \times 10^5 \left(5 \times 10^{12} - \frac{cq^2}{m}\right)$	$10^5 \left(7 \times 10^3 - \frac{b}{m}\right)$	$10^5 \left(5 \times 10^7 - \frac{k}{m}\right)$
Drop 3	$2 \times 10^4 \left(7 \times 10^{12} - \frac{cq^2}{m}\right)$	$2 \times 10^4 \left(1 \times 10^4 - \frac{b}{m}\right)$	$3 \times 10^4 \left(5 \times 10^7 - \frac{k}{m}\right)$

The only mode switching that occurs for this method is when the jet tip hits the substrate and breaks away from the tail. As in the previous method, a discrete drop in mass and charge occurs at this point, causing an instantaneous decrease in $\frac{cq^2}{m}$ and increase in $\frac{b}{m}$ and $\frac{k}{m}$. Table 4.5 gives the initial conditions which define the discrete change in parameter ratios at the beginning

of each drop mode. Note that the initial conditions for the first drop differ significantly from those of the second and third drops because the first drop begins near the nozzle. The charge and mass have already had time to build up at the jet tip, so all the initial parameter ratios are close to their final. The second and third drops begin at the substrate immediately following the jet tip break-off, so the initial mass and charge are much smaller. The parameter ratios require more time to build up to their final values.

Table 4.5 Initial conditions for parameter ratios in first, second, and third drop modes of a jetting cycle.

	$\left(\frac{cq^2}{m}\right)_i$	$\left(\frac{b}{m}\right)_i$	$\left(\frac{k}{m}\right)_i$
Drop 1	1×10^{12}	1×10^3	1×10^7
Drop 2	1×10^7	2.2×10^6	7×10^{10}
Drop 3	1×10^7	1.5×10^6	7×10^{10}

When the single-mode model is simulated using Stateflow, extra dummy “check” modes must be added after the second and third drop modes as shown in Figure 4.10. Because the switching condition is the same from each drop mode to the next, without the dummy mode, all of the drop modes would be skipped. The addition of this extra mode provides a check that to force the simulation to remain in the current drop mode until the switching condition is met again. The contents of each check mode are the same as those of the preceding drop mode. A retraction mode must be added at the end of the cycle to bring the jet back to the nozzle. The parameter ratios are set to constant values during the retraction.

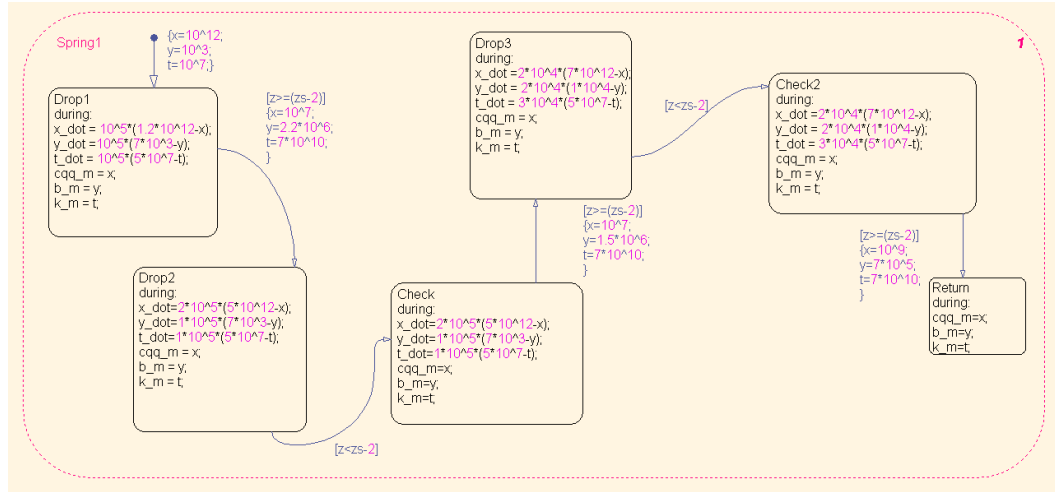


Figure 4.10 Stateflow diagram for determination of parameter ratio values during full jetting cycle with continuously changing parameter ratios.

Figure 4.11 shows the values of the parameter ratios during the simulation. Note that the parameters only undergo discrete changes when the jet reaches the substrate, and in between, they exhibit a first-order response.

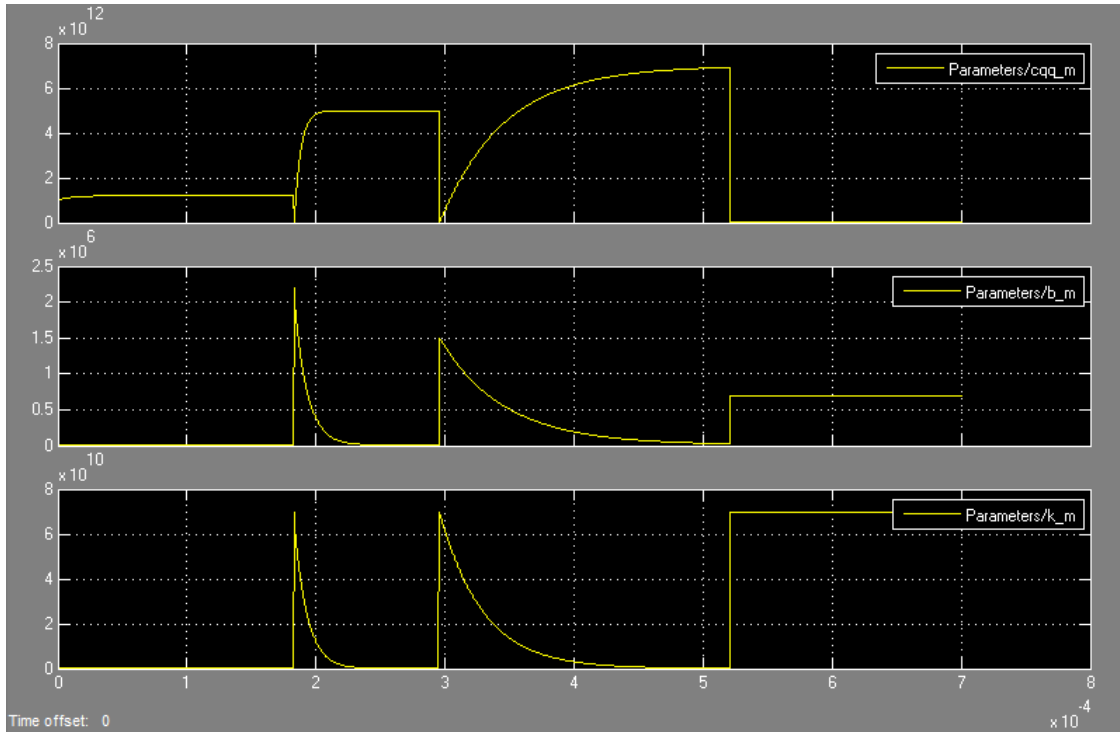


Figure 4.11 Parameter ratios during full jetting cycle simulation with three drop modes.

4.3.2 Results and Analysis

While the simulation results for this method do not precisely match those from the previous section, they are similar. The main difference is that there are no longer sharp transitions after retraction which were caused by the mode switch from the retraction mode to the build mode. The single-mode method described here fits the Test 5 data set because the time constants, initial conditions, and final values of the parameter ratios were chosen to match this data.

An important improvement that this single-mode method provides as compared to the three-mode method is that the only time a discrete change in parameters occurs is when the jet tip breaks away, leading to an instantaneous loss in mass and charge. There is no need to arbitrarily assign heights at which switching should occur except at the substrate.

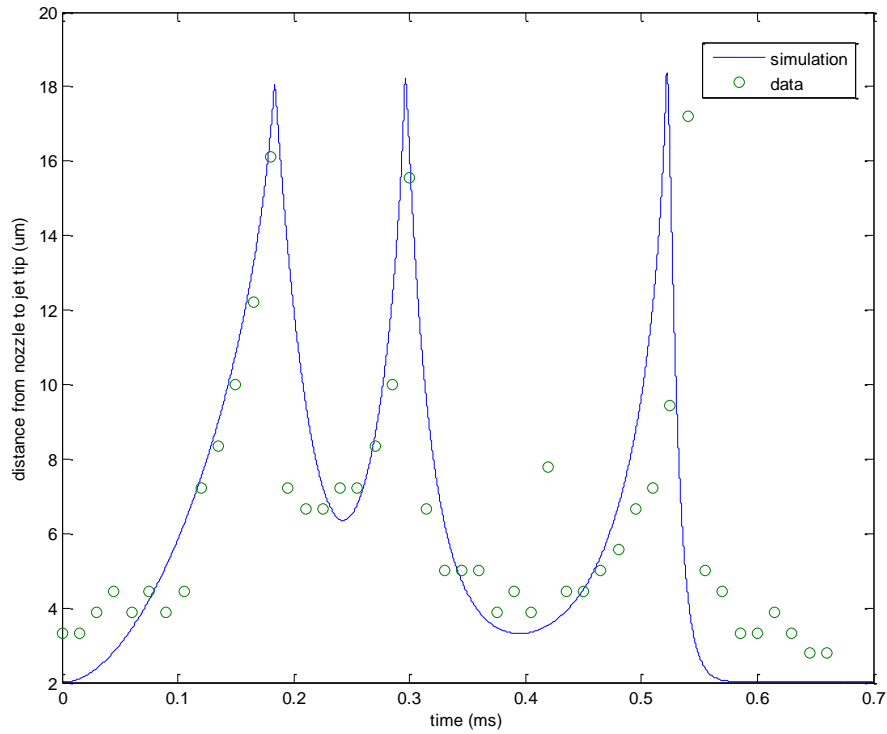


Figure 4.12 Height z of jet tip during a full jetting cycle from data and simulation using single-mode parameter model.

The simulation results are compared to the average height from all seventeen data sets in Figure 4.13. Again, for the first two drops, the simulated height lies within one standard deviation of the mean. For the third drop, the peak of the simulation results occurs slightly later than indicated by the data.

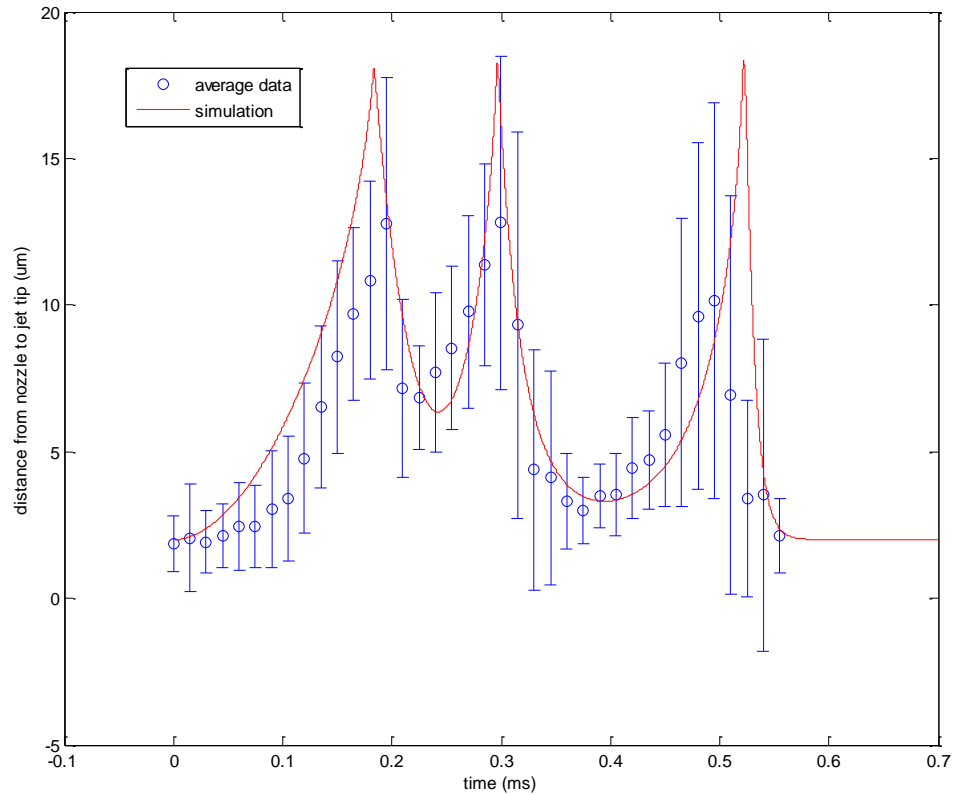


Figure 4.13 Comparison of height of jet tip during a full jetting cycle from simulation using single-mode parameter model and mean height during all data sets with error bars representing one standard deviation above and below the mean.

Because jet emission is an event-driven system rather than a time-driven system, there is some statistical variation in the timing of drops. The standard deviations shown above are large near the peaks because there is a slight variation in the timing of the drops from cycle to cycle. This creates a significant disparity for some time steps because a cycle with a peak at or near the time step has a large difference in height from a cycle with a peak slightly earlier or later. This also causes the average value to never reach the maximum distance reached in every test. A more

informative comparison can be found by plotting data from each test run and determining the test envelope by finding the upper and lower bounds of the data at each time step as in Figure 4.14. The simulation results fit well within this data envelope as shown in Figure 4.15.

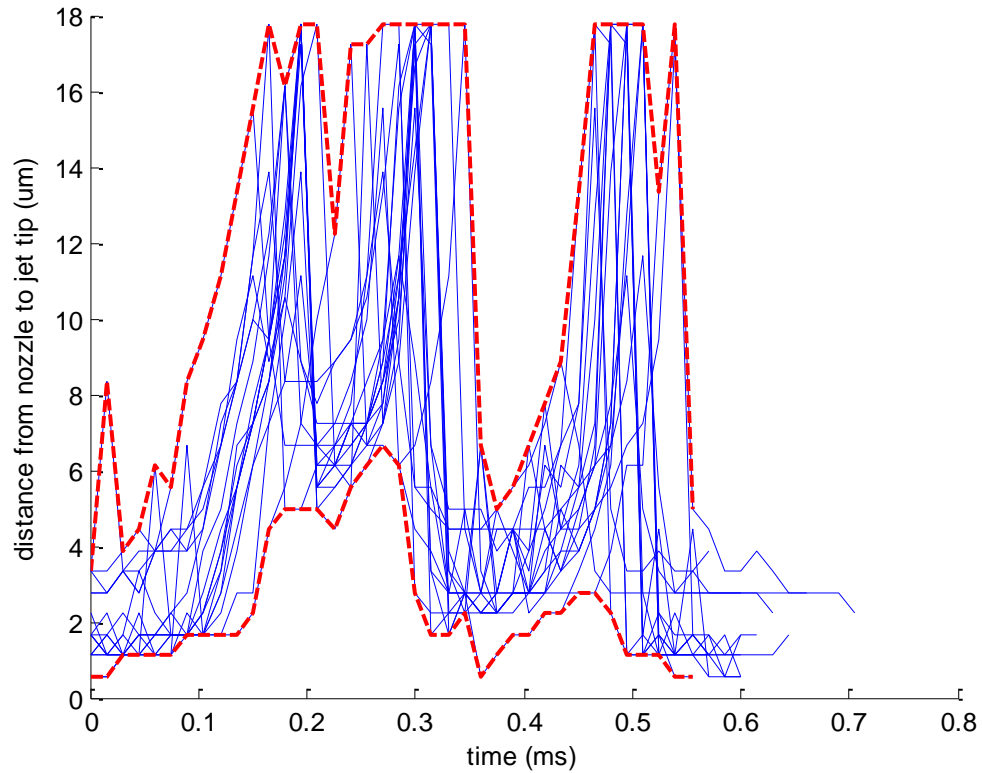


Figure 4.14 Height of jet tip during all seventeen jetting cycle tests with upper and lower bounds of data indicated by dashed line.

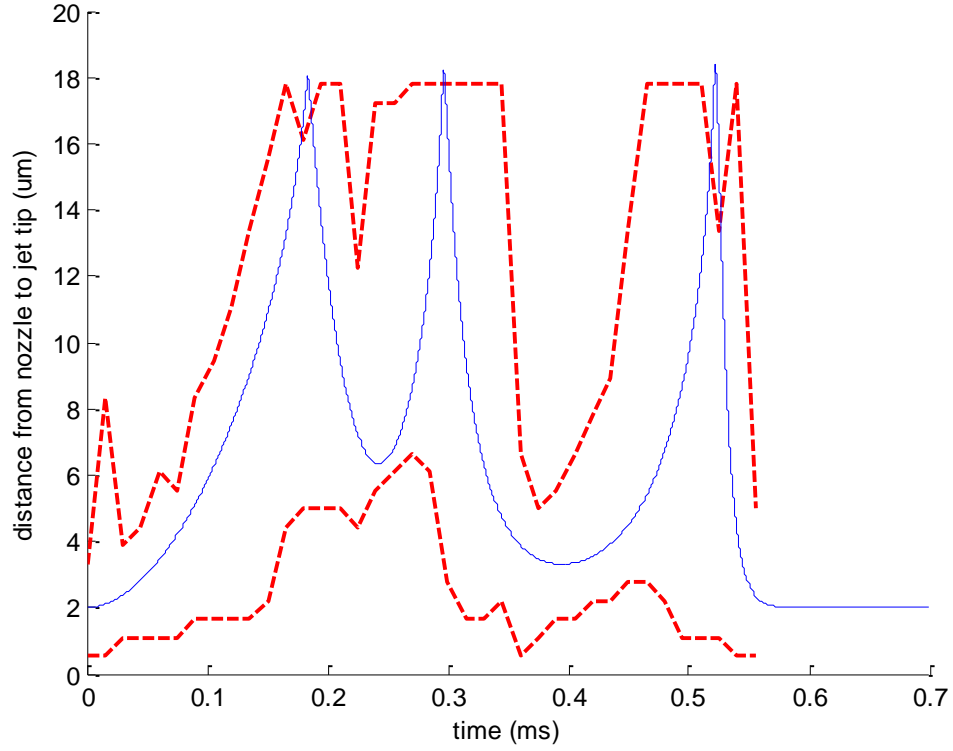


Figure 4.15 Comparison of height of jet tip during a full jetting cycle from simulation using single-mode parameter model and upper and lower bounds for envelope of data from all test runs.

4.4 Summary and Future Work

In this chapter, we proposed two different gray-box switched-system models for a multiple-drop jetting cycle. The first method includes drop, retraction, and build modes, while the second includes only a drop mode. While both models provide a good fit to the data, the second model also fits with the intuition that the only discrete change in parameters should occur when the tip of the jet breaks away as it reaches the substrate.

There remain some aspects of the jetting cycle which have not been explicitly included in our models. The modeling methods discussed in this chapter assume *a priori* knowledge of the number of drops produced in the jetting cycle. They do not allow us to predict the number of drops in a cycle for a particular system given a set of parameters. It is assumed that the jetting cycle ends because time is required to replace the ink at the nozzle tip, and until the ink is

replaced, the charge is insufficient to overcome the surface tension holding the ink to the nozzle. The balance between these effects can be described by the electrical Bond number [58]. An important next step in modeling the jetting cycle is to include a stopping criterion when the charge is not sufficient to produce a jet. On a related note, the cycle frequency is also related to the time required to refill the ink at the nozzle tip, build up the meniscus, and form a jet. A more complete model will include the ink refill and Taylor cone formation process. Our model is based on a system in which the jet tip does not break away from the tail until reaching the substrate. This is not necessarily true for all inks, and the relationship between ink properties and break-off height for a droplet should be investigated and included in the model to expand its ability to describe a wide variety of jetting behavior.

This gray-box model meets the need for a model that gives an accurate description of system behavior while providing a level of simplification that makes it potentially useful in multiple applications. With the addition of multiple nozzles spaced in close proximity, the speed of manufacturing can be increased. However, electrical interference between the nozzles can cause misplacement of drops as the trajectory of the jet is deflected [59]. With some modifications, our model can be used to predict the location of drop placement on the substrate by determining the trajectory with this interference taken into account. Because the model has proven to be useful in predicting the position of the jet tip for multiple test cycles, investigation into pulse shapes other than constant voltage or square pulses can be tested in simulation and the best pulse shape can then be applied to the physical system. Testing pulse shapes in simulation can potentially reduce the amount of time to select a pulse shape as compared to running many experiments and analyzing the data. Another area where the model could be useful is in the selection of inks based on properties for applications with particular requirements. Some additional study is needed to relate ink properties to the system parameters we have defined, but the ability to select inks based on properties would be beneficial. For example, when printing at high speeds, an ink that produces multiple drops per jetting cycle may cause some misplaced extra drops. This model could allow the user to select an ink with only one drop per cycle. The accuracy and simplicity of the model will allow it to be used in a wide variety of applications for the improvement of E-jet printing.

Chapter 5

Conclusions

5.1 Summary

In this thesis, we have demonstrated improvements to E-jet printing in two areas: conductive ink printing and modeling of the jetting cycle.

In Chapter 2, two new silver nanoparticle inks from UT Dots (AgHB and AgDDB) were printed. Some of the challenges involved with printing these and other conductive inks included: nozzle clogging due to ink aging, solvent evaporation, and too high a concentration of silver; line breaks during printing or annealing; lack of conductivity due to the lack of thickness in the lines; and unevenness in line thickness due to the coffee ring effect. Solutions or ways to avoid these issues were presented, and narrow ($<5\text{ }\mu\text{m}$) conductive lines were printed. Resistivity for the printed lines is approximately ten times the resistivity of bulk silver, which is acceptable for many applications of printed electronics.

In Chapter 3, we proposed a relatively simple gray box model for the height of a jet tip during printing based on a mass-spring-damper system analogy for the jet tip and tail. High-speed videos of the printing of a model ink, NOA 74, were captured and analyzed to determine the height of the jet tip during its trajectory. The batch least squares method was used to fit the parameters of the second-order model based on the data during a single drop from the nozzle to the substrate. The parameters were tuned to provide a slightly better fit, and the resulting height predicted by the model matched the data closely.

Chapter 4 expanded on the mass-spring-damper model proposed in Chapter 3 to account for the position of the jet tip during a full jetting cycle. Two models were proposed. In the first,

the jet is considered to go through multiple drop, retraction, and build modes in a complete cycle. The parameters are constant during the drop and retraction modes, and change linearly during the build mode. Discrete parameter changes occur when the jet tip breaks away due to instantaneous loss of mass and charge. In order to match the data, this model requires arbitrary switching based on knowledge of the actual system behavior, and counterintuitive discrete parameter changes must be included. In order to eliminate these issues, a second model was proposed. This model is based on a single drop mode in which parameters exhibit a first-order response. Switching only occurs when the jet tip breaks away, and discrete parameter changes still occur at these events. This model provides an accurate description of the system behavior as validated by comparing the simulated height of the jet tip to the average height over data collected for all cycles.

5.2 Conclusions

The silver inks demonstrated in this work may be directly applied in E-jet printing of electronic devices and circuits. The resistivity is sufficiently low so that printed lines will be useful for interconnects, and the ability to print lines of width less than 5 μm with low resistivity provides a step forward compared to previous results. Additionally, the discussion of problems and solutions for conductive ink printing in general will be useful for other researchers desiring to develop other inks, particularly metal nanoparticle inks.

The gray-box modeling for the jetting cycle can be used to better understand the E-jet printing process. With additional study on the relationship between system parameters and ink properties, it can also be used to predict the trajectory of jets produced by any arbitrary ink. While the jet cycle model developed in this work is useful on its own, it will be even more powerful when combined with models which describe other facets of the E-jet printing process including the buildup of charge in the meniscus, development of the Taylor cone, and charge-vs.-surface tension threshold for jetting. We have also demonstrated the ability of a simplified model to accurately reproduce the system behavior in a more general sense. While the model structure chosen in this work provides a good representation of the system, it is by no means the only model which may be used. The gray-box modeling technique of selecting and imposing a simplified yet intuitively reasonable model structure and matching the system parameter values

based on the data may be applied to develop other models for jetting behavior as required by other researchers.

5.3 Future Work

The work from Chapter 2 on silver printing should be extended by incorporating the silver ink we have demonstrated into complete electronic devices. Printed conductive lines can function as interconnects between devices or components. An example of E-jet printed interconnects used to connect LEDs is shown in Figure 5.1. The LEDs were created with a transfer printer, and silver ink was used to print interconnects and pads between them. The ink shown in this image is a commercial inkjet ink from Inktec Corp. A voltage was applied across the pads to light up the LEDs. While the line quality is poor, the functionality of the interconnects is clear. By using AgDDB ink, we can print connecting lines and pads to the LEDs in the same way shown here, but the width of the lines can be reduced and the quality can be improved. The ink from UT Dots can also be used in other electronic devices, including transistors.

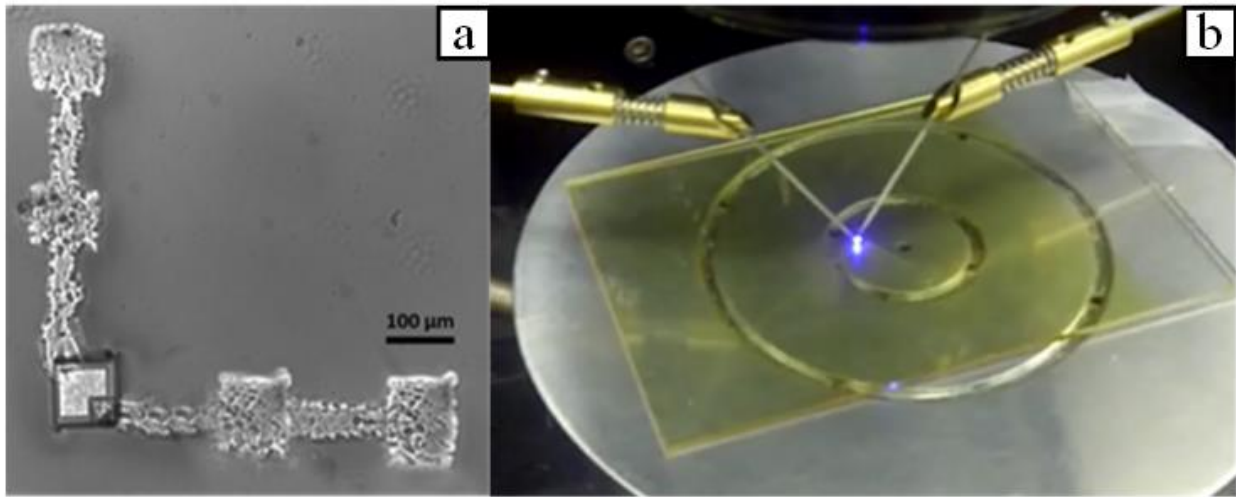


Figure 5.1 Demonstration of silver interconnects printed with E-jet, (a) showing magnified LED and interconnects and (b) showing LED response to voltage difference applied across printed pads.

The modeling efforts from Chapters 3 and 4 can be expanded by incorporating models which describe other salient features of the printing process to give a more complete picture.

Additionally, the relationship between system parameters and ink properties needs further study. This will facilitate prediction of the jet tip trajectory based on ink properties and allow selection of an ink which will meet the needs of a particular application. The model we have developed can also be used to simulate interference effects between multiple nozzles and to determine the effects of various pulse shapes on the jet cycle.

List of References

- [1] (2011, Jan. 3). *The State of Manufacturing in the United States*. [Online]. Available: http://trade.gov/manufactureamerica/facts/tg_mana_003019.asp#P13_602
- [2] J. P. Holdren, “A National Strategic Plan for Advanced Manufacturing,” 2012.
- [3] Busnaina, A. “Introduction to Nanoscale Manufacturing and the State of the Nanomanufacturing Industry in the United States” in *Nanomanufacturing Handbook*. Boca Raton, FL: CRC Press, 2007, ch. 1, sec. 1.2, pp. 4-5.
- [4] M. A. Meitl, Z.-T. Zhu, V. Kumar, K. J. Lee, X. Feng, Y. Y. Huang, I. Adesida, R. G. Nuzzo, and J. A. Rogers, “Transfer printing by kinetic control of adhesion to an elastomeric stamp,” *Nature Materials*, vol. 5, no. 1, pp. 33–38, Dec. 2005.
- [5] P. Calvert, “Inkjet Printing for Materials and Devices,” *Chemistry of Materials*, vol. 13, no. 10, pp. 3299–3305, Oct. 2001.
- [6] M. Singh, H. M. Haverinen, P. Dhagat, and G. E. Jabbour, “Inkjet printing-process and its applications,” *Advanced Materials*, vol. 22, no. 6, pp. 673–85, Mar. 2010.
- [7] L. Setti, C. Piana, S. Bonazzi, B. Ballarin, D. Frascaro, A. Fraleoni-Morgera, and S. Giuliani, “Thermal Inkjet Technology for the Microdeposition of Biological Molecules as a Viable Route for the Realization of Biosensors,” *Analytical Letters*, vol. 37, no. 8, pp. 1559–1570, Dec. 2004.
- [8] G. Taylor, “Disintegration of water drops in an electric field,” *Proceedings of the Royal Society of London. Series A, Mathematical and Physical Sciences*, vol. 280, no. 1382, pp. 383–397, 2013.
- [9] J.-U. Park, M. Hardy, S. J. Kang, K. Barton, K. Adair, D. K. Mukhopadhyay, C. Y. Lee, M. S. Strano, A. G. Alleyne, J. G. Georgiadis, P. M. Ferreira, and J. A. Rogers, “High-resolution electrohydrodynamic jet printing,” *Nature Materials*, vol. 6, no. 10, pp. 782–9, Oct. 2007.
- [10] T. Someya, T. Sekitani, S. Iba, Y. Kato, H. Kawaguchi, and T. Sakurai, “A large-area, flexible

- pressure sensor matrix with organic field-effect transistors for artificial skin applications,” *Proceedings of the National Academy of Sciences of the United States of America*, vol. 101, no. 27, pp. 9966–70, Jul. 2004.
- [11] L. Zhou, A. Wanga, S.-C. Wu, J. Sun, S. Park, and T. N. Jackson, “All-organic active matrix flexible display,” *Applied Physics Letters*, vol. 88, no. 8, p. 083502, 2006.
- [12] J. Choi, Y.-J. Kim, S. Lee, S. U. Son, H. S. Ko, V. D. Nguyen, and D. Byun, “Drop-on-demand printing of conductive ink by electrostatic field induced inkjet head,” *Applied Physics Letters*, vol. 93, no. 19, p. 193508, 2008.
- [13] K. Barton, “Precision Coordination and Motion Control of Multiple Systems via Iterative Learning Control,” Ph.D. dissertation, University of Illinois at Urbana-Champaign, Urbana, IL, 2010.
- [14] K. Barton, S. Mishra, K. Alex Shorter, A. Alleyne, P. Ferreira, and J. Rogers, “A desktop electrohydrodynamic jet printing system,” *Mechatronics*, vol. 20, no. 5, pp. 611–616, Aug. 2010.
- [15] E. Sutanto, K. Shigeta, Y. K. Kim, P. G. Graf, D. J. Hoelzle, K. L. Barton, A. G. Alleyne, P. M. Ferreira, and J. A. Rogers, “A multimaterial electrohydrodynamic jet (E-jet) printing system,” *Journal of Micromechanics and Microengineering*, vol. 22, no. 4, p. 045008, Apr. 2012.
- [16] C.-H. Chen, D. A. Saville, and I. A. Aksay, “Scaling laws for pulsed electrohydrodynamic drop formation,” *Applied Physics Letters*, vol. 89, no. 12, p. 124103, 2006.
- [17] R. T. Collins, J. J. Jones, M. T. Harris, and O. A. Basaran, “Electrohydrodynamic tip streaming and emission of charged drops from liquid cones,” *Nature Physics*, vol. 4, no. 2, pp. 149–154, Dec. 2007.
- [18] G. E. Moore, “Cramming more components onto integrated circuits,” *Electronics Magazine*, vol. 38, no. 8, 1975.
- [19] H.-H. Lee, K.-S. Chou, and K.-C. Huang, “Inkjet printing of nanosized silver colloids,” *Nanotechnology*, vol. 16, no. 10, pp. 2436–41, Oct. 2005.
- [20] D. Kim, S. H. Lee, S. Jeong, and J. Moon, “All-Ink-Jet Printed Flexible Organic Thin-Film Transistors on Plastic Substrates,” *Electrochemical and Solid-State Letters*, vol. 12, no. 6, p. H195, 2009.
- [21] C. Kim, M. Nogi, and K. Suganuma, “Electrical conductivity enhancement in inkjet-printed narrow lines through gradual heating,” *Journal of Micromechanics and Microengineering*, vol. 22, no. 3, p. 035016, Mar. 2012.
- [22] S. Molesa, D. R. Redinger, D. C. Huang, and V. Subramanian, “High-quality inkjet-printed

- multilevel interconnects and inductive components on plastic for ultra-low-cost RFID applications,” *Materials Research Society Symposium Proceedings*, vol. 769, pp. 1–6, 2003.
- [23] Z. Yin, Y. Huang, N. Bu, X. Wang, and Y. Xiong, “Inkjet printing for flexible electronics: Materials, processes and equipments,” *Chinese Science Bulletin*, vol. 55, no. 30, pp. 3383–3407, Nov. 2010.
- [24] S. E. Burns, P. Cain, J. Mills, J. Wang, and H. Sirringhaus, “Inkjet Printing of Polymer Thin-Film Transistor Circuits,” *MRS Bulletin*, no. November, pp. 829–834, 2003.
- [25] D. Kim, S. Jeong, S. Lee, B. K. Park, and J. Moon, “Organic thin film transistor using silver electrodes by the ink-jet printing technology,” *Thin Solid Films*, vol. 515, no. 19, pp. 7692–7696, Jul. 2007.
- [26] D.-Y. Lee, J.-C. Lee, Y.-S. Shin, S.-E. Park, T.-U. Yu, Y.-J. Kim, and J. Hwang, “Structuring of conductive silver line by electrohydrodynamic jet printing and its electrical characterization,” *Journal of Physics: Conference Series*, vol. 142, p. 012039, Dec. 2008.
- [27] A. Khan, K. Rahman, M.-T. Hyun, D.-S. Kim, and K.-H. Choi, “Multi-nozzle electrohydrodynamic inkjet printing of silver colloidal solution for the fabrication of electrically functional microstructures,” *Applied Physics A*, vol. 104, no. 4, pp. 1113–1120, Apr. 2011.
- [28] S. Khan, Y. H. Doh, A. Khan, A. Rahman, K. H. Choi, and D. S. Kim, “Direct patterning and electrospray deposition through EHD for fabrication of printed thin film transistors,” *Current Applied Physics*, vol. 11, no. 1, pp. S271–S279, Jan. 2011.
- [29] K. H. Choi, M. Mustafa, K. Rahman, B. K. Jeong, and Y. H. Doh, “Cost-effective fabrication of memristive devices with ZnO thin film using printed electronics technologies,” *Applied Physics A*, vol. 106, no. 1, pp. 165–170, Nov. 2011.
- [30] T. Sekitani, Y. Noguchi, U. Zschieschang, H. Klauk, and T. Someya, “Organic transistors manufactured using inkjet technology with subfemtoliter accuracy,” *Proceedings of the National Academy of Sciences of the United States of America*, vol. 105, no. 13, pp. 4976–80, Apr. 2008.
- [31] “Realization of Low-resistance Ultra-fine Copper Wires Using an Inkjet Technology”, National Institute of Advanced Industrial Science and Technology, Tsukuba, Ibaraki, Japan, 2011.
- [32] D. J. Lee, J. H. Oh, and H. S. Bae, “Crack formation and substrate effects on electrical resistivity of inkjet-printed Ag lines,” *Materials Letters*, vol. 64, no. 9, pp. 1069–1072, May 2010.
- [33] J. Perelaer, C. E. Hendriks, A. W. M. de Laat, and U. S. Schubert, “One-step inkjet printing of conductive silver tracks on polymer substrates,” *Nanotechnology*, vol. 20, no. 16, p. 165303, Apr.

2009.

- [34] K. Wang, M. D. Paine, and J. P. W. Stark, "Fully voltage-controlled electrohydrodynamic jet printing of conductive silver tracks with a sub-100 μm linewidth," *Journal of Applied Physics*, vol. 106, no. 2, p. 024907, 2009.
- [35] D.-Y. Lee, Y.-S. Shin, S.-E. Park, T.-U. Yu, and J. Hwang, "Electrohydrodynamic printing of silver nanoparticles by using a focused nanocolloid jet," *Applied Physics Letters*, vol. 90, no. 8, p. 081905, 2007.
- [36] *UTDAg Conductive Silver Nanoinks* [Online]. Available: <http://www.utdots.com/page5.html>
- [37] J.-K. Jung, S.-H. Choi, I. Kim, H. C. Jung, J. Joung, and Y.-C. Joo, "Characteristics of microstructure and electrical resistivity of inkjet-printed nanoparticle silver films annealed under ambient air," *Philosophical Magazine*, vol. 88, no. 3, pp. 339–359, Jan. 2008.
- [38] J. R. Greer and R. A. Street, "Thermal cure effects on electrical performance of nanoparticle silver inks," *Acta Materialia*, vol. 55, no. 18, pp. 6345–6349, Oct. 2007.
- [39] F. Lacy, "Developing a theoretical relationship between electrical resistivity, temperature, and film thickness for conductors," *Nanoscale Research Letters*, vol. 6, no. 1, p. 636, Jan. 2011.
- [40] D. Dayal, P. Rudolf, and P. Wibmann, "Thickness dependence of the electrical resistivity of epitaxially grown silver films," *Thin Solid Films*, vol. 79, pp. 193–199, 1981.
- [41] D. Janssen, R. De Palma, S. Verlaak, P. Heremans, and W. Dehaen, "Static solvent contact angle measurements, surface free energy and wettability determination of various self-assembled monolayers on silicon dioxide," *Thin Solid Films*, vol. 515, no. 4, pp. 1433–1438, Dec. 2006.
- [42] R. D. Deegan, O. Bakajin, and T. F. Dupont, "Capillary flow as the cause of ring stains from dried liquid drops," *Nature*, vol. 389, pp. 827–829, 1997.
- [43] D. Kim, S. Jeong, B. K. Park, and J. Moon, "Direct writing of silver conductive patterns: Improvement of film morphology and conductance by controlling solvent compositions," *Applied Physics Letters*, vol. 89, no. 26, p. 264101, 2006.
- [44] D. Soltman and V. Subramanian, "Inkjet-printed line morphologies and temperature control of the coffee ring effect," *Langmuir*, vol. 24, no. 5, pp. 2224–31, Mar. 2008.
- [45] E. Sutanto, "Design and Fabrication of Multimaterial Electrohydrodynamic-Jet Deposition System," M.S. thesis, University of Illinois at Urbana-Champaign, Urbana, IL, 2011.
- [46] J. R. Sheats, "Manufacturing and commercialization issues in organic electronics," *Journal of*

Materials Research, vol. 19, no. 07, pp. 1974–1989, Mar. 2011.

- [47] P.-H. Chen, H.-Y. Peng, H.-Y. Liu, S.-L. Chang, T.-I. Wu, and C.-H. Cheng, “Pressure response and droplet ejection of a piezoelectric inkjet printhead,” *International Journal of Mechanical Sciences*, vol. 41, no. 2, pp. 235–248, Feb. 1999.
- [48] I. Marginean, L. Parvin, L. Heffernan, and A. Vertes, “Flexing the electrified meniscus: the birth of a jet in electrosprays,” *Analytical chemistry*, vol. 76, no. 14, pp. 4202–7, Jul. 2004.
- [49] C.-H. Chen, D. a. Saville, and I. A. Aksay, “Scaling laws for pulsed electrohydrodynamic drop formation,” *Applied Physics Letters*, vol. 89, no. 12, p. 124103, 2006.
- [50] W. Deng and A. Gomez, “Full transient response of Taylor cones to a step change in electric field,” *Microfluidics and Nanofluidics*, vol. 12, no. 1–4, pp. 383–393, Sep. 2011.
- [51] R. T. Collins, K. Sambath, M. T. Harris, and O. A. Basaran, “Universal scaling laws for the disintegration of electrified drops,” *Proceedings of the National Academy of Sciences of the United States of America*, vol. 110, no. 13, pp. 4905–10, Mar. 2013.
- [52] Y. Oussar and G. Dreyfus, “How to be a gray box: dynamic semi-physical modeling,” *Neural networks : the official journal of the International Neural Network Society*, vol. 14, no. 9, pp. 1161–72, Nov. 2001.
- [53] P. Martien, S. Pope, P. Scott, and R. Shaw, “The chaotic behavior of the leaky faucet,” *Physics Letters*, vol. 110A, no. 7, 8, pp. 399–404, 1985.
- [54] K. Kiyono and N. Fuchikami, “Dripping Faucet Dynamics by an Improved Mass-Spring Model,” *Journal of the Physical Society of Japan*, vol. 68, no. 10, pp. 3259–3270, 1999.
- [55] A. D’Innocenzo, F. Paladini, and L. Renna, “Experimental study of dripping dynamics,” *Physical Review E*, vol. 65, no. 5, p. 056208, Apr. 2002.
- [56] G. Sánchez-Ortiz and A. Salas-Brito, “Strange attractors in a relaxation oscillator model for the dripping water faucet,” *Physics Letters A*, vol. 203, pp. 300–311, 1995.
- [57] J. Brunahl and A. M. Grishin, “‘Chevron’-type piezoelectric inkjet actuator,” in *Proceedings of the 13th IEEE International Symposium.*, 2002, pp. 491–494.
- [58] O. Basaran and L. E. Scriven, “Axisymmetric Shapes and Stability of Pendant and Sessile Drops in an Electric Field,” *Journal of Colloid and Interface Science*, vol. 140, no. 1, pp. 10–30, 1990.
- [59] J.-S. Lee, S.-Y. Kim, Y.-J. Kim, J. Park, Y. Kim, J. Hwang, and Y.-J. Kim, “Design and evaluation of a silicon based multi-nozzle for addressable jetting using a controlled flow rate in

electrohydrodynamic jet printing,” *Applied Physics Letters*, vol. 93, no. 24, p. 243114, 2008.